Star Formation Activity in the Long, Filamentary Infrared Dark Cloud G53.2

Hyun-Jeong Kim[1] and Bon-Chul Koo[2]

Department of Physics and Astronomy, Seoul National University, Seoul 151-742, Korea

and

Christopher J. Davis[3]

Astrophysics Research Institute, Liverpool John Moores University, Liverpool, L3 5RF, UK

ABSTRACT

We present star formation activity in the infrared dark cloud (IRDC) G53.2, a remarkable IRDC located at Galactic coordinates $(l, b) \sim (53^\circ.2, 0^\circ.0)$ based on the census of young stellar object (YSO) candidates. IRDC G53.2 was previously identified as several IRDCs in mid-IR images, but it is in fact a long ($\gtrsim$45 pc) cloud, well consistent with a CO cloud at $v \sim 23$ km s^{-1} (or at $d \sim$1.7 kpc). We present a point-source catalog of IRDC G53.2 that contains ∼370 sources from our photometry of the *Spitzer* MIPS 24 μm data and Galactic Legacy Infrared Mid-Plane Survey Extraordinaire Catalog. The classification of the identified sources based on their spectral index and control field analysis to remove field star contamination reveals that IRDC G53.2 is an active star-forming region with ∼300 YSO candidates. We compare the YSO classification based on spectral index, mid-IR colors, and the wavelength range used, which results in consistent classification, except for flat-spectrum objects, with some ambiguity between Class I and II. Comparison of the YSO population in IRDC G53.2 with those of other nearby star-forming clusters indicates that they are similar in age; on the other hand, stronger association with mid-IR stellar sources in IRDC G53.2 compared with other IRDCs indicates that IRDC G53.2 is at a later evolutionary stage among IRDCs. Spatial distribution of the YSO candidates in IRDC G53.2 shows a good correlation with ^{13}CO column density and far-IR emission, and earlier-class objects tend to be more clustered in the regions with higher density.

Subject headings: infrared: stars — ISM: clouds — stars: formation — stars: pre-main sequence

[1]hjkim@astro.snu.ac.kr

[2]koo@astro.snu.ac.kr

[3]c.j.davis@ljmu.ac.uk

1. Introduction

Massive stars ($M \gtrsim 8M_{\odot}$) have a great influence in the interstellar medium and the galactic environment by providing ionizing photons and kinetic energy, enriching heavy elements, and so on. Nonetheless, compared with low-mass stars, the formation process of massive stars still remains unclear because direct observations of high-mass protostars are challenging owing to their rarity, long distances, and short lifetimes. Infrared dark clouds (IRDCs), which are identified as silhouettes against the bright Galactic background in mid-IR, are cold (<20 K) and very dense (>10^5 cm^{-3}) clouds with high column densities ($\sim 10^{21}$–10^{23} cm^{-2}; Carey et al. 1998, 2000; Egan et al. 1998; Pillai et al. 2006; Peretto & Fuller 2010; Ragan et al. 2011). Thus, IRDCs are believed to be the precursors to massive stars and star clusters. Millimeter/far-IR clumps/cores found in IRDCs with masses from a few tens to thousands of solar masses support this (e.g., Rathborne et al. 2006; Henning et al. 2010), while the investigation of star formation in the IRDC at Galactic coordinates $(l, b) \sim (48^{\circ}.66, -0^{\circ}.30)$ using *Spitzer* data (van der Wiel & Shipman 2008) showed a diverse distribution in the mass of young stellar objects (YSOs), with no massive (>8 $M_{\odot}$) ones, although their sample size was small (<20).

Since IRDCs were cataloged from the *Midcourse Space Experiment* (*MSX*) 8 μm data (MSXDC catalog; Simon et al. 2006a) and more recently from the *Spitzer* Galactic Legacy Infrared Mid-Plane Survey Extraordinaire (GLIMPSE; Benjamin et al. 2003)[1] 8 μm data (Peretto & Fuller 2009), several studies on physical properties and star formation characteristics of IRDCs via multiwavebands from mid- and far-IR to radio have been published (e.g., Rathborne et al. 2006; Simon et al. 2006b; Chambers et al. 2009; Battersby et al. 2010; Jackson et al. 2010). Most studies have mainly focused on statistical properties of IRDCs/IRDC clumps themselves or star formation activities on clump or core scales rather than on a stellar scale represented by mid-IR detection. The IRDCs in the previous studies are composed of several clumps in a diverse mass range (Ragan et al. 2009; Henning et al. 2010), and as IRDC clumps evolve, they tend to be more associated with star formation tracers, including mid-IR (24 μm) stellar sources (Chambers et al. 2009; Battersby et al. 2010). However, only a small fraction of IRDC clumps that have thus far been investigated are associated with 24 μm emission features (Ragan et al. 2009). The number of 24 μm stellar sources in IRDCs is usually very limited (van der Wiel & Shipman 2008; Henning et al. 2010), too few for a proper statistical analysis of star formation in individual IRDCs after the clumps (i.e., the precursors to massive stars and clusters) further fragment. Therefore, an investigation on IRDCs with many young stars (i.e., large number of stellar sources detected in mid-IR) such as the one presented in this study and comparison with star formation activities in other well-studied star-forming regions are crucial to understanding the statistical properties of star formation (e.g., YSO population, star formation rate, or initial mass function) in IRDCs.

In this paper, we present star formation activity in an IRDC located at Galactic coordinates

[1]http://www.astro.wisc.edu/glimpse/glimpsedata.html

$(l, b) \sim (53°.2, 0°.0)$. This IRDC (IRDC G53.2, hereafter) is long and filamentary, extending $\gtrsim 1°$ in the mid-IR images as seen in Figure 1, and it shows a number of bright mid-IR stellar sources distributed along its filamentary structure. IRDC G53.2 was previously identified as three separate IRDCs in the MSXDC catalog (MSXDC G053.11+00.05, MSXDC G053.25+00.04, MSXDC G053.31+00.00; Simon et al. 2006a) as presented in Figure 1, and as 56 IRDCs in the *Spitzer* IRDC catalog (Peretto & Fuller 2009); however, we have found that these individual IRDCs in the previous two catalogs lying between $l \sim 53°$ and $54°$ are well consistent with a CO cloud at $v \sim 23$ km s^{-1}. Therefore, in this study, we consider these separate IRDCs in the mid-IR image to be associated, and we investigate the overall star formation activity in IRDC G53.2 using a catalog of YSO candidates constructed from *Spitzer* data. This paper is organized as follows. In Section 2, we define IRDC G53.2 based on the associated molecular cloud and present its physical parameters. In Section 3, we describe the point-source catalog (PSC) of IRDC G53.2, followed by selection and classification of YSO candidates in Section 4 and accounting for contaminations in Section 5. We then discuss different schemes of YSO classification, the characteristics of star formation in IRDC G53.2 in terms of the stellar population, and spatial distribution of the YSO candidates in Section 6. In Section 7, we give our summary and conclusions.

2. Molecular Cloud Associated with IRDC G53.2

IRDC G53.2, seen as several separate filamentary clouds in the mid-IR images (Figure 1), coincides with a CO cloud at $v \sim 23$ km s^{-1}. We use the ^{13}CO $J = 1$–0 data from the Boston University−Five College Radio Astronomy Observatory Galactic Ring Survey (GRS; Jackson et al. 2006) to determine the distance and the mass of IRDC G53.2. Figure 2 shows the integrated intensity and the mean velocity distributions of the ^{13}CO emission in the area of IRDC G53.2. We integrate the GRS cube data from 15 to 30 km s^{-1}, which covers essentially all of the CO emission associated with the cloud (see the average spectrum of the cloud in the inset of Figure 2). In Figure 2, the cloud is elongated over $\sim 1°.5$ long in the Galactic plane (for the cloud size determination, see below), but we note that the CO cloud at low brightness level extends as far as $\gtrsim 2°.4$. The mean velocity of the cloud varies from 22 to 24 km s^{-1} from the western to the eastern part of the cloud (Figure 2), and the mean velocity of the entire cloud is +22.9 km s^{-1}. Assuming a flat rotation curve with $R_\odot = 8.5$ kpc and $\Theta_\odot = 220$ km s^{-1}, the kinematic distance to the cloud is 1.7 kpc, and we adopt this as the distance to IRDC G53.2.[2]

In order to obtain the mass of IRDC G53.2, we first derive the ^{13}CO column density ($N(^{13}\mathrm{CO})$) map. In principle, the integrated intensity map in Figure 2 can be converted to an $N(^{13}\mathrm{CO})$ map if the excitation temperature (T_{ex}) is known under the LTE assumption (e.g., Rohlfs & Wilson 2000).

[2]For comparison, Ragan et al. (2014) identified the same molecular cloud in their study of filamentary molecular clouds (F54.0−52.0 in their Table 1) and assigned a kinematic distance of 2.0 kpc using the Galactic rotation model of Reid et al. (2009), which is based on high-mass star-forming regions.

One may assume that $T_{\rm ex}$ is equal to the observed brightness temperature of the ^{12}CO $J = 1$–0 emission, which is usually optically thick, but there are uncertainties associated with this method such as unknown beam-filling factors or pointing/calibration errors from different observations. In addition, the available ^{12}CO $J = 1$–0 data from the Massachusetts−Stony Brook (UMSB) Galactic Plane Survey (Clemens et al. 1986; Sanders et al. 1986) are rather poorly sampled. We therefore instead adopt $T_{\rm ex} = 10$ K which is a typical excitation temperature of IRDCs determined from CO observations (Heyer et al. 2009; Roman-Duval et al. 2010; Liu et al. 2014). (The median $T_{\rm ex}$ from these works might be somewhat below 10 K, e.g., 8–9 K.) We note that, however, $T_{\rm ex} = 10$ K may be too low for some regions in IRDC G53.2. The main-beam brightness temperature ($T_{\rm mb}$) of the ^{13}CO $J = 1$–0 line is given as $T_{\rm mb} = (J_\nu(T_{\rm ex}) - J_\nu(T_{\rm bg}))(1 - \exp(-\tau_{13}))$, where $J_\nu(T) = 5.29/(\exp(5.29/T) - 1)$, $T_{\rm bg} = 2.73$ K, and τ_{13} is the optical depth of ^{13}CO $J = 1$–0 emission (e.g., Rohlfs & Wilson 2000). Assuming $T_{\rm ex} = 10$ K and $\tau_{13} = 3$, which is a typical optical depth for most IRDCs (Liu et al. 2014), the maximum allowed $T_{\rm mb}$ of the ^{13}CO $J = 1$–0 line is 6.4 K, whereas toward the cloud cores (e.g., areas around 1.2 mm contours in Figure 1) $T_{\rm mb}$ is higher than this, in some regions as high as 20 K. The excitation temperature in these areas also must be high, and the ^{13}CO emission might be optically thick, which is not unusual for IRDCs (e.g., Liu et al. 2014). We indeed confirmed that the ^{13}CO line intensities are comparable to the ^{12}CO line intensities in these areas from the UMSB data. Therefore, we derive the $N(^{13}{\rm CO})$ map of IRDC G53.2 by applying different assumptions for inner and outer areas of the cloud. For the outer areas with $T_{\rm mb} \leq 6.4$ K, we assume $T_{\rm ex} = 10$ K, while for the inner areas with $T_{\rm mb} \geq 6.4$ K, instead of assuming $T_{\rm ex}$, we assume a constant optical depth of $\tau_{13} = 3$. This is an ad hoc method but will provide a smooth and reasonable $N(^{13}{\rm CO})$ map until a more accurate map is obtained from detailed molecular line studies. (The resulting $N(^{13}{\rm CO})$ map is found in Figure 9.)

The $N(^{13}{\rm CO})$ map is then converted to a mass density map assuming $^{12}{\rm C}/^{13}{\rm C} = 60$ (Milam et al. 2005, their Equation (3)) and $n(^{12}{\rm CO})/n({\rm H_2}) = 1.1 \times 10^{-4}$ (Pineda et al. 2010). The total mass of the cloud depends on how we fix its outer boundary. For the analysis of the star formation activity in this study, we define the boundary of IRDC G53.2 by the ^{13}CO integrated intensity contour at $\int T_{\rm mb} dv = 6.3$ K km s^{-1} (Figure 1), which corresponds to $N(^{13}{\rm CO}) \sim 1 \times 10^{16}$ cm^{-2}. This boundary is chosen such that the IRDC includes the dark filamentary features seen in mid-IR (24 μm) but excludes bright emission nebulosities at 8 and 24 μm, which are likely foreground regions, to avoid contamination from unrelated mid-IR sources as much as possible. Adopting the boundary at $N(^{13}{\rm CO}) = 1 \times 10^{16}$ cm^{-2}, the cloud mass is $6.2 \times 10^4 M_\odot$, with a mean mass surface density of 0.076 g cm^{-2}. The cloud, however, has a low-density envelope (Figure 2), and we account for this by adopting $N(^{13}{\rm CO}) = 3 \times 10^{15}$ cm^{-2} (the ^{13}CO integrated intensity contour at $\int T_{\rm mb} dv \sim 2.1$ K km s^{-1}) or $A_V = 1$ mag as the cloud boundary, which is slightly beyond the outermost contour in Figure 2. This yields an entire cloud mass of $1.0 \times 10^5 M_\odot$ and a mean surface density of 0.033 g cm^{-2}.[3] The derived parameters of IRDC G53.2 are listed in Table 1.

[3]Ragan et al. (2014) obtained $6.8 \times 10^4 M_\odot$ as the mass of the molecular cloud.

3. PSC of IRDC G53.2

We make a PSC of IRDC G53.2 region to search for YSO candidates. We use two *Spitzer* inner Galactic plane surveys as a major data set in this study: GLIMPSE and MIPS GALactic plane survey (MIPSGAL; Carey et al. 2009). These *Spitzer* legacy programs cover the inner Galactic plane at the four IRAC bands of 3.6, 4.5, 5.8, and 8.0 μm (GLIMPSE) and the two MIPS bands of 24 and 70 μm (MIPSGAL). Other published catalogs such as the Two Micron All Sky Survey (2MASS) PSC (Skrutskie et al. 2006)[4] and *MSX* PSC (Egan et al. 2003)[5] are also used as complements.

3.1. Point-source Photometry of MIPS 24 μm Mosaics

We perform point-source photometry of MIPSGAL 24 μm data to extract point sources in IRDC G53.2 since our first criterion to build a PSC of the IRDC G53.2 area is the presence of 24 μm emission. We start with four 24 μm mosaics centered at $(l, b) = (53°.0, 0°.5)$, $(53°.0, -0°.5)$, $(54°.0, 0°.5)$, and $(54°.0, -0°.5)$, which are distributed by MIPSGAL v3.0 Data Delivery.[6] The size of each mosaic is $1°.1 \times 1°.1$, and the pixel size is $1''.25$. We use the Astronomical Point source EXtractor (APEX) software in the MOsaicking and Point-source EXtraction (MOPEX) package developed at the *Spitzer* Science Center[7] to extract point sources and compute photometry by the point response function (PRF) fitting method based on Recipe 24 of the *Spitzer* Data Analysis Cookbook.[8] We first extract bright sources in the background-subtracted mosaics generated by taking a median filter of the images with an 11 pixel by 11 pixel filter and remove the Airy rings around the bright sources so that the Airy rings are not detected as faint objects; subsequently, we extract faint sources from the above images. We measure the flux of the extracted sources and scale them, following the Cookbook, by a factor of 1.46 to correct lost fluxes due to a small background filter size. The magnitude zero point we use to convert the estimated fluxes to magnitudes is 7.14 Jy as reported in the MIPS Data Handbook v.3.2.1.

The number of sources within the boundary of IRDC G53.2 presented in Figure 1 from the above procedure is 844. Here we exclude the sources within the GRS ^{13}CO contour at $(l, b) \sim (53^{\circ}.2, 0^{\circ}.2)$ in Figure 1. Although the contour level is the same in the integrated intensity map, its lower ($\lesssim$20 km s^{-1}) velocity compared to the other region of the IRDC (see Figure 2) and bright emission in 24 μm indicate that the sources in this region are unlikely associated with IRDC G53.2. Among the 844 sources in the IRDC, the faintest source is 8.41 mag, and the magnitude from which

[4]http://www.ipac.caltech.edu/2mass/releases/allsky

[5]http://heasarc.gsfc.nasa.gov/W3Browse/all/msxpsc.html

[6]http://irsa.ipac.caltech.edu/data/SPITZER/MIPSGAL

[7]http://irsa.ipac.caltech.edu/data/SPITZER/docs/dataanalysistools/tools/mopex

[8]http://irsa.ipac.caltech.edu/data/SPITZER/docs/dataanalysistools/cookbook

the number of sources drops is ∼7.8 mag. Since the background emission around the IRDC region is bright and complicated, we do not extract fainter sources for reliability.

3.2. Merging with GLIMPSE Catalog

The 24 μm sources from the PRF photometry are then matched to the GLIMPSEI v2.0 Catalog and Archive with a matching radius of 2″ to make a PSC of the IRDC G53.2 area. As mentioned above, the 24 μm mosaics have complicated background emissions, so residual emissions in the background-subtracted mosaics are sometimes detected as a source during the point-source extraction process. After matching the sources, we remove the false ones by visual inspection comparing the original and background-subtracted mosaics. Finally, 369 sources out of 844 are matched with the GLIMPSEI Catalog or Archive. Table 2 presents the coordinates and IR magnitudes of the 369 matched sources. The number of sources whose IRAC magnitudes are from the GLIMPSEI Archive is 51, and we put a superscript *"a"* to their classes in column 13 (see Section 4 for the source classification). From the PRF photometry by APEX, we only get uncertainties from the fitting, whereas there is an absolute uncertainty (4% for 24 μm) from the pipeline calibration according to MIPS Instrument Handbook v.3.[9] Therefore, we add both in quadrature and present in Table 2. Note that the 24 μm errors in Table 2 are underestimated because they do not account for uncertainties from other components such as background variations. Since we choose completeness rather than reliability, we do not make any criteria for using the GLIMPSEI Catalog/Archive. The median uncertainty of the IRAC-band magnitudes of the sources in Table 2 is 0.053 mag, and $\lesssim$ 9% of the sources have any one of the IRAC-band magnitudes with its error $\gtrsim$0.2 mag.

Because of strong and complicated background emission, many of the unmatched sources are probably false detections arising from the residuals after removing the Airy rings or from extended emission. There may be genuine sources as well that are very deeply embedded, e.g., Class 0 YSOs. Those not detected in the IRAC bands, however, are beyond the scope of this study, so we do not further examine the unmatched sources here. We note that one of the unmatched sources at (R.A., decl.) = (19:29:16.18, +17:56:10.32) is very bright at 24 μm, with its magnitude of 1.04 mag, but not detected in any IRAC bands. Our new recent observation in near-IR using adaptive optics reveals that this source is, in fact, composed of two stars separated by ∼0″.75 (H.-J.Kim et al., in preparation). We measure its IRAC band fluxes from aperture photometry, but extended features, particularly remarkable at 5.8 and 8.0 μm, make the measured fluxes less reliable; therefore, we exclude this source from our catalog.

[9]http://irsa.ipac.caltech.edu/data/SPITZER/docs/mips/mipsinstrumenthandbook

3.3. Final Point-source Catalog

From the MIPS 24 μm mosaics and GLIMPSE Catalog/Archive, 369 sources in total are identified in IRDC G53.2 and listed in Table 2. Among them, 302 sources are also identified in 2MASS PSC, so we include their 2MASS magnitudes in Table 2 (columns 4–6).

There are four saturated sources in the MIPS 24 μm mosaics that are not extracted by APEX. For these sources, we use MSX PSC as a complement to their IRAC 8 μm and MIPS 24 μm magnitudes. The 2MASS and IR magnitudes of these four sources with their coordinates from the 2MASS PSC are presented in Table 3. Note that No. 2 is so close to No. 1 that it is not resolved in the data from *MSX*, which has a larger beam size than *Spitzer*.

4. Selection and Classification of YSO Candidates

We select and classify YSO candidates in our PSC (Table 2) based on the IR spectral index defined as $\alpha = d\,\log(\lambda F_\lambda)/d\,\log(\lambda)$ (Lada 1987). Spectral index can be used to quantify the slope of spectral energy distributions (SEDs) of YSOs in the IR and to divide YSOs into several classes. We compute the spectral index of each object in Table 2 by least-squares linear fitting between 2 and 24 μm. Among 369 sources, we only fit 347 sources that are detected in more than three IRAC bands to make enough data points and classify them as follows (Greene et al. 1994; Billot et al. 2010): $0.3 \leq \alpha$ as Class I, the youngest evolutionary class whose SED is rising toward mid-IR, which indicates the presence of a dusty envelope infalling onto a central protostar; $-1.6 \leq \alpha < -0.3$ as Class II, which are pre-main-sequence stars with warm optically thick dusty disks; $-2.56 \leq \alpha < -1.6$ as Class III, objects whose SED is mostly photospheric emission in near-IR but which show some excess emission at longer (>20 μm) wavelengths; and $\alpha < -2.56$ as photospheric-emission-only (photospheric, hereafter) sources. We also include flat-spectrum ($-0.3 \leq \alpha < 0.3$), whose evolutionary status is likely between Class I and II, although flat-spectrum sources could be considered as Class I (e.g., Calvet et al. 1994). The computed spectral indices α with 1σ errors and the results of classification are presented in Table 2 (columns 12 and 13). We also compute the spectral indices of the MIPS-saturated sources using available data and present their α and classes in Table 3 (columns 12 and 13).

As a next step, we examine the sources that are excluded from the fitting owing to insufficient data. If a source is bright in 24 μm but not detected in shorter wavebands, it is possible that the source is deeply embedded. In the investigation of the young, embedded cluster NGC 1333, Gutermuth et al. (2008) suggested that any source that lacks detections in some IRAC bands but is bright at MIPS 24 μm ($[24] < 7$ and $[X] - [24] > 4.5$ mag, where $[X]$ is the photometry for any IRAC detection available) is likely a deeply embedded protostar. Following this, we check 22 sources detected in only one or two IRAC bands and find that 16 sources satisfy the criterion above. Nondetection of these deeply embedded protostars in the IRAC bands may indicate that they are Class 0 protostars, which are very young accreting protostars in an earlier evolutionary phase than

Class I (André 2002). However, Class 0 protostars are not distinguishable from Class I objects by using α (Evans et al. 2009), and Class 0 protostars are originally defined by submillimeter flux (André 2002). Since we concentrate on mid-IR properties of YSOs, an exact classification of Class 0 protostars is not necessary in this study; therefore, we include the deeply embedded protostars in Class I and put a superscript *"d"* to their classes in Table 2. The remaining six sources that do not meet the criterion for deeply embedded protostars are classified as 'No Class' sources in the table.

Finally, among 373 sources in IRDC G53.2, including the saturated sources (two Class I and two Class II objects) in the MIPS 24 μm (Tables 2 and 3), we find 78 Class I (21%), 66 flat-spectrum (18%), 135 Class II (36%), 62 Class III (17%), and 26 photospheric (7%) sources, leaving 6 ($\sim$ 1%) sources without classification. In further sections, we refer to Class I, flat-spectrum, Class II, and Class III objects as YSO candidates.

5. Contaminations

5.1. Extragalactic Contamination

MIPS sources generally contain extragalactic backgrounds as well as Galactic sources, but we expect most sources in IRDC G53.2 to be Galactic since the IRDC is in the Galactic plane ($b \sim 0^{\circ}$). Although both galaxies and YSOs show IR-excess emission, they can be distinguished in a [3.6] versus [3.6]$-$[24] plot (Rebull et al. 2011). In the [3.6] versus [3.6]$-$[24] plot, Rebull et al. (2011) compared the extragalactic sources from the *Spitzer* Wide-area Infrared Extragalactic Survey (SWIRE; Lonsdale et al. 2003) European Large Area *ISO* Survey (ELAIS) N-1 extragalactic field with the YSO candidates in North American and Pelican Nebulae (NAN) and Serpens (see their Figure 10), and they found that the YSO candidates occupy a different region from the SWIRE-type contaminants, which include galaxies and diskless stars. We also compare the IRDC G53.2 sources (Tables 2 and 3) with the SWIRE ELAIS N-1 samples[10] in Figure 3. In the figure, the distribution of the IRDC 53.2 sources (colored circles) is distinctively separated from the SWIRE-field samples (gray dots) except for the ones with mostly stellar photospheric emission (i.e., Class III and photospheric sources), which have [3.6]$-$[24]$\sim$0. The location of the YSO candidates in IRDC G53.2 in the [3.6] versus [3.6]$-$[24] plot is similar to those of the YSO candidates in NAN and Serpens as well (Figure 10 of Rebull et al. 2011). In addition, we searched the SIMBAD database[11] and found no counterpart for each of our 373 sources among known extragalactic sources within a 5$''$ radius. We therefore conclude that essentially all of our sources are likely of Galactic origin, and there is very little contamination from extragalactic sources.

---

[10]SWIRE ELAIS N1 Region 24 μm Spring '05 Spitzer Catalog from IPAC Infrared Science Archive (http://irsa.ipac.caltech.edu/applications/Gator)

[11]http://simbad.u-strasbg.fr/simbad/

5.2. Field Star Contamination

While we do not expect extragalactic contamination toward the Galactic plane, there is nonetheless contamination by foreground/background stars. In order to account for the amount of contamination from these field stars, we analyze control fields and compare the population of point sources between the control fields and IRDC G53.2. We select seven control fields around IRDC G53.2 where there are no CO clouds in the GRS ^{13}CO $J = 1$–0 data. The control fields in the GRS integrated intensity map are presented in Figure 4 by white ellipses and circles with their numbers. In the figure, the integration of the GRS cube data has been done over the entire velocity range of the GRS survey, i.e., $v_{\rm LSR} = -5$ to $+85$ km s^{-1}, and the scale bar indicates the integrated intensity scale. The boundary of IRDC G53.2 is shown by a black contour as well.

We identify point sources in the control fields from the MIPS 24 μm mosaic, match them to the GLIMPSEI Catalog/Archive, and perform the same spectral index analysis as we did for the sources in IRDC G53.2. In the seven control fields, 218 sources are classified in total. Table 4 presents the results of the control field analysis and the comparison to IRDC G53.2. Among the sources in the control fields (column 2), about 90% are Class III or photospheric sources with little excess emission in IR. The others classified as Class I, flat-spectrum, or Class II show similar IR excess to the YSO candidates. These IR-excess sources are, however, not likely YSOs but the sources with similar colors to YSOs such as AGB stars or planetary nebulae because they are mostly isolated and placed where there are no molecular clouds. Since the area of the IRDC is $\lesssim$0.5 times of the total area of the control fields, we scale the number of sources in the control fields to the IRDC G53.2 area to compute the expected numbers of each class (column 3) and compare them with the numbers of the sources in the IRDC (column 4).

The comparison between the control fields and IRDC G53.2 implies that there is a negligible contamination from field stars in earlier classes of YSO candidates (i.e., Class I, flat-spectrum, and Class II), while about 50% of field star contamination exists among Class III objects. In addition, all photospheric sources identified in the IRDC G53.2 area are not likely the genuine members of the IRDC but foreground/background stars. We note that we detect fewer ($\lesssim$50%) photospheric sources in IRDC G53.2 than expected from the control field analysis. Photospheric sources without strong IR excess are mostly faint in 24 μm; for example, the median [24] magnitudes of each class in IRDC G53.2 are 4.5, 6.2, 6.8, 7.1, and 7.7 for Class I, flat-spectrum, Class II, Class III, and photospheric objects, respectively. Since the extinction toward IRDC G53.2 is higher than the control fields without molecular clouds, we probably have failed to detect a large number of photospheric sources owing to extinction, which results in a smaller number of the photospheric sources in the IRDC compared to the scaled number from the control fields. Here, we only compare the sources with the MIPS 24 μm photometry (Table 2) because there are no saturated sources in the MIPS 24 μm mosaic in the control regions. However, even if we include the MIPS-saturated sources that are presented in the parentheses in column 4 of Table 4, its small number does not affect the results.

Based on the comparison with the control fields, we expect that our PSC of IRDC G53.2 is contaminated with 1 Class I, 3 flat-spectrum, 6 Class II, and 29 Class III objects. All of the photospheric sources in our catalog are likely to be contaminants. If we removed this field star contamination, we would be left with 308 sources in total (including four MIPS-saturated sources), and the final census of YSO candidates would be 77 Class I (25%), 63 flat-spectrum (21%), 129 Class II (42%), 33 Class III (11%) objects, and 6 No Class (1%) sources.

6. Discussion

6.1. Classification Schemes of YSOs

6.1.1. Based on Spectral Index, α

In classification of YSOs, an empirical scheme based on the slope of SEDs was first constructed by Lada & Wilking (1984) and more quantitatively developed by Lada (1987) adopting the definition of spectral index α. Since then, Greene et al. (1994), introducing flat-spectrum (see Section 3.1), has developed the classification system in the study of the ρ Oph YSO population. Whereas the original definition of α used wavelengths between 2 and 20 μm (Lada & Wilking 1984), several recent studies have used only the four IRAC bands to compute α (e.g., Lada et al. 2006; Billot et al. 2010). Regarding differences in the choice of wavelength range, Greene et al. (1994) claimed no deviation between α computed using 2.2–20 μm and 2.2–10 μm, but Evans et al. (2009) classified YSOs in five nearby molecular clouds in the c2d project (Evans et al. 2003, hereafter the c2d clouds) using both 2–24 μm and the IRAC bands and showed that using only the IRAC bands moves sources from earlier to later classes, resulting in 10%–15% difference in inferred lifetimes for the earlier SED phases.

In Section 4, we classified the point sources in IRDC G53.2 by least-squares linear fitting between 2 and 24 μm. In order to examine the difference in classification depending on the use of wavelength range, we classify the sources again using only the IRAC bands and compare the results to the one we have from 2–24 μm in Figure 5. In Figure 5, the histogram of spectral index from only using the IRAC bands, drawn in red, shows a relatively lower number of flat-spectrum and higher number of Class III than the histogram of spectral index from 2–24 μm, drawn in black. When using only the IRAC bands, we get fewer Class I (by $\sim$7%), fewer flat-spectrum (by $\sim$40%), comparable Class II, and more Class III (by $\sim$43%). Since a direct comparison in numbers of each class does not account for uncertainties from fitting in the computation of spectral index, we show a spectral index from 2–24 μm ($\alpha_{2-24\mu\mathrm{m}}$) versus spectral index from the IRAC bands (α_{IRAC}) plot with their 1σ uncertainties from fitting in Figure 6. As shown in Figure 6, most sources plotted by gray circles have consistent classes from the both spectral indices. Red squares in Figure 6 are the sources that are classified as earlier class by α_{IRAC} with its fraction of $\sim$7%, but they fall into the same classes by $\alpha_{2-24\mu\mathrm{m}}$ when accounting for uncertainty. Blue triangles in the figure are the

sources that are classified as later class by $\alpha_{\rm IRAC}$ with its fraction of $\sim$20%; however, if we account for the uncertainties, the fraction of sources classified by later class by $\alpha_{\rm IRAC}$ is 12%. From the above comparison, the uncertainty in YSO candidate classification in this study from the choice of wavelength range in determination of spectral index will be $\sim$12%.

6.1.2. Based on Mid-infrared Colors

YSOs are often classified based on mid-IR colors. For example, Gutermuth et al. (2008, 2009) established a mid-IR color-based method that can robustly distinguish YSOs and mitigate the effects of contamination and reddening. Their mid-IR color-based method primarily uses the IRAC magnitudes/colors and additionally uses 24 μm detection for further classifying "Transition Disk" Class II sources, deeply embedded protostars, and highly reddened Class II sources. The color-based classification of YSOs in principle relies on the mid-IR excess emission, as the spectral-index-based classification does, but different criteria between the two may give different classification. In order to check this possibility, we apply the classification scheme described in Gutermuth et al. (2009) to the sources in IRDC G53.2 and compare the results between the color-based and the $\alpha_{2-24\mu{\rm m}}$-based classification. Among 369 sources in Table 2 (excluding the saturated sources in 24 μm), 70 and 189 sources are classified as Class I and Class II, respectively, based on mid-IR colors, where Class I includes 16 deeply embedded protostars and Class II includes 52 transition disk sources and 7 highly reddened Class II sources. The others are the sources with photospheric colors or the sources that lack the IRAC magnitudes. Comparing the number of objects in each class, we find that most Class I ($\gtrsim$80%), Class II (>90%), and Class III/photospheric sources ($\sim$100%) from the $\alpha_{2-24\mu{\rm m}}$-based classification are well consistent with the color-based classes. In the case of flat-spectrum sources, however, $\sim$80% are classified as Class II by the color-based classification, while they are supposed to be included in Class I according to Gutermuth et al. (2009).

A possible reason for this discrepancy is an ambiguity of flat-spectrum. Since flat-spectrum is an evolutionary stage between Class I and Class II, separating flat-spectrum sources from either class will be highly uncertain. The wavelength range used in classification can be a reason as well. Although the color-based classification is made from IRAC to MIPS 24 μm wavelengths, classes are mainly determined by IRAC colors because the 24 μm magnitudes are only additionally used to classify anomalies such as transition disk or highly reddened Class II. Therefore, a source with an SED slope in the IRAC wavelengths close to the boundary between flat-spectrum and Class II but bright in 24 μm may be classified as Class II by the color-based scheme, whereas it would be classified as flat-spectrum (i.e., Class I) by the $\alpha_{2-24\mu{\rm m}}$-based scheme. This trend is also seen in the comparison between the $\alpha_{2-24\mu{\rm m}}$-based and $\alpha_{\rm IRAC}$-based classification discussed above (Section 6.1.1). We note that extinction may be an another factor that moves flat-spectrum to Class II, and it will be discussed below in detail. In summary, the mid-IR color-based classification of YSOs is consistent with the $\alpha_{2-24\mu{\rm m}}$-based classification scheme in general, except when classifying flat-spectrum sources. In such objects, there is some ambiguity between Class I and Class II

sources, which is likely dependent on the wavelength ranges used. The difference between the two classifications will affect the number ratio of Class II to Class I objects by a factor of two or three (Section 6.2.1).

6.1.3. Based on Physical Properties of SEDs

On the other hand, Robitaille et al. (2006) adopted a "Stage" classification. Stage is based on the physical properties of SEDs, thus referring to the actual evolutionary stage rather than Class, which is only based on the slope of SEDs. Although Stage 0/I/II/III is analogous to Class 0/I/II/III, it is not a one-to-one correspondence because of the inclination effect. For example, pre-main-sequence stars with an "edge-on" disk can be classified as flat-spectrum or Class I by their SED slopes, and Crapsi et al. (2008), in their study on the nature of embedded YSOs using radiative transfer modeling, claimed that 34% of the Stage II sources could be misclassified as flat-spectrum. Despite the possible misclassification, however, the classes of the YSO candidates in IRDC G53.2 classified based on spectral index $\alpha_{2-24\mu\mathrm{m}}$ agree fairly well with the stages in a color-color diagram as presented in Figure 7. In Figure 7, Class I, II, and III objects mostly fall into the areas of Stage I, II, and III (Robitaille et al. 2006), respectively. Flat-spectrum sources again show an ambiguity between Stages I and II, but ∼65% are located in the Stage I area. The others placed in the Stage II area may represent the ones with large inclination angle. Comparison of "Class" and "Stage" classification from the [3.6]−[5.8] versus [8.0]−[24] color-color diagram indicates a general agreement between the two, although there are some exceptions. Detailed investigation on the physical properties of the YSO candidates in IRDC G53.2 based on the analysis of the individual SEDs will be addressed in our forthcoming paper.

6.1.4. Effects from Extinction on Classification

Embedded star-forming regions in a dense molecular cloud suffer high extinction from dust and reddening. High column density, and thus high extinction, toward IRDC G53.2 may affect the classification of YSOs based on SED shapes, but it may not be significant because of much smaller extinction in mid-IR than in optical. Previous studies using *Spitzer* data also show that the effects from extinction on the overall YSO classification are small. Evans et al. (2009) compared spectral index of YSOs in the c2d clouds before and after extinction correction and found that the effect from extinction was small (10%–20%), probably smaller than other sources of uncertainty. Billot et al. (2010) also found that the YSO census in the Vulpecula OB association (hereafter Vul OB1) based on the mid-IR color method showed only a marginal difference after they corrected for extinction. This indicates that classification schemes based on mid-IR excess are only moderately affected by extinction. However, it is also possible that extinction effects in our analysis of the IRDC G53.2 YSO population, which is much further away and embedded in a denser molecular cloud, may not be as negligible as in the above studies, and we will briefly discuss expected effects

from extinction on the YSO census in IRDC G53.2 below.

The local extinction in star-forming regions may be derived using the near-IR colors of stars observed in each region and comparing these with their intrinsic colors (e.g., Evans et al. 2009; Gutermuth et al. 2009). However, since this method is limited to nearby regions, we cannot apply it to IRDC G53.2. Extinction in IRDC G53.2 is also not uniform; it is larger in the central parts of the molecular cloud, where the ^{13}CO integrated intensity map peaks in Figure 2 (left). To investigate the effects of extinction on our YSO census, we therefore consider the extreme case of one of the clumps in IRDC G53.2 (from Butler & Tan 2012) and examine how it could possibly affect the YSO classes. Butler & Tan (2012) estimated physical properties of starless and early-stage cores and clumps in 10 IRDCs, including the one in IRDC G53.2 (MSX G053.11+00.05 in Figure 1; core J1 in Butler & Tan 2012) based on the mid-IR extinction mapping technique. Their estimation, using the IRAC 8 μm images, gave a mean mass surface density of $\sim$0.15 g cm^{-2} or $\tau_{8\mu\mathrm{m}} \sim 1.1$ (according to their Equation (1)) for a clump in the *MSX* G053.11+00.05. From the mid-IR extinction law derived by *Spitzer* data (Flaherty et al. 2007; Chapman et al. 2009), we estimate the extinction at each IRAC and MIPS 24 μm band as follows, although extinction at 24 μm is highly uncertain owing to a small sample size in Flaherty et al. (2007) and Chapman et al. (2009): $A_{[3.6]} = 1.6$–1.7 mag, $A_{[4.5]} = 1.3$–1.4 mag, $A_{[5.8]} \sim 1.2$ mag, $A_{[8.0]} \sim 1.2$ mag, and $A_{[24]} \sim 1$ mag. If we apply extinction correction to these values in Figure 7, about half of the flat-spectrum sources in the Stage I area move to the Stage II area, whereas Class I and Class II sources show only a small changes. However, we note that this extinction will be close to the upper limit in IRDC G53.2. The clump in the *MSX* G053.11+00.05 is located where the ^{13}CO emission is strong, corresponding to the innermost contour in Figure 2, and extinction of most of the area in the IRDC should be much lower. For example, the mass surface density (or extinction) of the outer part of the clump in the *MSX* G053.11+00.05 is $\sim$10% of the mean value (Figure 12 of Butler & Tan 2012), which does not make any remarkable changes in Figure 7. Therefore, extinction in IRDC G53.2 may affect the YSO classification in a way to decrease the number of flat-spectrum objects and increase the number of Class II objects, but the effect on the overall classification is likely insignificant.

6.2. Comparison of the YSO Population in IRDC G53.2 to Other Regions

While IRDCs are believed to be a probable site of massive star formation, many of them do not show a signature of active star formation in mid-IR represented by 24 μm point sources (Chambers et al. 2009), and the clumps in IRDCs are typically not associated with 24 μm sources (Ragan et al. 2009). In this aspect, IRDC G53.2, with a few hundreds of YSO candidates, is a unique place where we can statistically investigate the stellar population formed in IRDCs. The YSO population in IRDC G53.2 is also able to provide the star formation activity occurring in the whole associated molecular cloud in which IRDCs are embedded. Below, we discuss the stellar population in IRDC G53.2 by comparing with that of other well-studied star-forming regions in different environments

(Section 6.2.1). We also compare with other IRDCs, some of which are associated with 24 μm sources and some of which are not (Section 6.2.2), mainly focusing on the evolutionary stage of the IRDC. Finally, we estimate the age of IRDC G53.2 using an analytic model (Myers 2012) based on the YSO census and compare it with other nearby star-forming clusters (Section 6.2.3).

6.2.1. Comparison with Other Star-forming Regions: Number Ratio of Class II to Class I

We first compare the census of YSO candidates in IRDC G53.2 and other star-forming regions because the number of YSOs in each class can provide an estimation of the relative age of a star-forming region, assuming a constant birthrate (Gutermuth et al. 2009). For example, the number ratio of Class II to Class III objects, which can be a diagnostic of a fraction of YSOs with disks (i.e., disk fraction), gives the age of a star-forming region since disk fraction exponentially decreases with the age of a star-forming region (Mamajek 2009; Ybarra et al. 2013). The use of the ratio of Class II to Class III, however, would be inappropriate in the case of IRDC G53.2. In IRDC G53.2, the fraction of Class I and flat-spectrum sources that may not even form accretion disks is rather high ($\lesssim$50%), and the census of Class III objects and photospheric sources is likely to be incomplete because of their weak IR-excess emission and faintness at 24 μm (see Section 5.2). Instead, we use the number ratio of Class II to Class I objects ($N_{\rm ClassII}/N_{\rm ClassI}$, hereafter) to compare the relative age of IRDC G53.2 with other star-forming regions. As mentioned in Section 4, the evolutionary status of flat-spectrum is rather uncertain, and the objects with SEDs of flat-spectrum are often included in Class I if they are not separately classified (e.g., Gutermuth et al. 2009). Following this, we include flat-spectrum in Class I in the discussion below.

Figure 8(a) presents $N_{\rm ClassII}/N_{\rm ClassI}$ of IRDC G53.2 and other star-forming regions from the literature. In the figure, $N_{\rm ClassII}/N_{\rm ClassI}$ of IRDC G53.2, which is 0.9 after removing field star contamination, is marked with a filled red star, and the ratios of other star-forming regions from different literature are marked with different filled symbols. Filled gray circles are from a systematic *Spitzer* survey on 36 young, nearby, star-forming clusters within 1 kpc by Gutermuth et al. (2009), and a gray dashed line indicates the median value of $N_{\rm ClassII}/N_{\rm ClassI}$ (3.7) for these clusters. $N_{\rm ClassII}/N_{\rm ClassI}$ of the c2d clouds (Evans et al. 2009) and Vul OB1 (Billot et al. 2010) are also presented by a filled blue square and filled purple downward-pointing triangle, respectively. Filled green triangles are $N_{\rm ClassII}/N_{\rm ClassI}$ of YSOs that are spatially associated with dark filamentary structures in the inner Galactic region of $10^\circ < l < 15^\circ$ and $-1^\circ < b < 1^\circ$ using GLIMPSE data (Bhavya et al. 2013). While nearby, low-mass star-forming regions (Evans et al. 2009; Gutermuth et al. 2009) and Vul OB1 (Billot et al. 2010) show higher $N_{\rm ClassII}/N_{\rm ClassI}$ than that of IRDC G53.2, YSOs likely related to IRDCs (Bhavya et al. 2013) show similar or lower $N_{\rm ClassII}/N_{\rm ClassI}$ compared to IRDC G53.2. Direct comparison of the number ratios from different studies, however, is not appropriate because (1) different classification schemes affect the fraction of each class, as discussed in Section 6.1, and (2) different distances affect the detection limit so that the number of faint sources at 24 μm (i.e., later-class YSOs) decreases as the distance to the star-forming region increases.

To make an appropriate comparison, we first compute $\alpha_{2-24\mu m}$ of YSOs in the star-forming clusters from Gutermuth et al. (2009) and Vul OB1 (Billot et al. 2010) using their flux catalogs and reclassify them. Gutermuth et al. (2009) classified YSOs using their mid-IR colors. Since the color-based classification results in fewer Class I and more Class II sources than the $\alpha_{2-24\mu m}$-based classification (Section 6.1.2), $N_{\rm ClassII}/N_{\rm ClassI}$ will become higher if one uses the color-based classification scheme. After reclassification of their sources based on $\alpha_{2-24\mu m}$, the median of $N_{\rm ClassII}/N_{\rm ClassI}$ for all the clusters becomes smaller, as expected, from 3.7 to 2.0. New $N_{\rm ClassII}/N_{\rm ClassI}$ distribution and the median value are presented in Figure 8(b) with filled gray circles and a gray dashed line, respectively. Billot et al. (2010) classified the YSOs in Vul OB1 using $\alpha_{\rm IRAC}$, so they also have fewer flat-spectrum and more Class II sources and thus higher $N_{\rm ClassII}/N_{\rm ClassI}$ (Section 6.1.1 and Figure 5). Our $\alpha_{2-24\mu m}$-based classification scheme to the sources in Vul OB1 decreases $N_{\rm ClassII}/N_{\rm ClassI}$ from 1.9 to 1.2, and the new ratio is marked with an open purple downward-pointing triangle in Figure 8(b). For the c2d clouds (Evans et al. 2009), we use their results because they used $\alpha_{2-24\mu m}$ in classification.

Next, we correct for distance by assuming that the nearby regions from Evans et al. (2009) and Gutermuth et al. (2009) are at the same distance as IRDC G53.2 (at 1.7 kpc). To do this, we scale the fluxes of the YSOs and extract the sources brighter than a threshold at 24 μm. For the threshold, we use 8.41 mag, the faintest 24 μm magnitude in IRDC G53.2. Larger distance may affect the classification itself as well owing to higher extinction, but such an effect will be negligible in the overall statistics (Section 6.1.4). We mark distance-corrected $N_{\rm ClassII}/N_{\rm ClassI}$ in Figure 8(b) using open orange circles for the clusters in Gutermuth et al. (2009) with their median value of 0.8 (orange dashed line) and an open blue square for the c2d clouds. For the clusters in Gutermuth et al. (2009), we only consider the clusters with total number of YSOs > 10. In the c2d clouds, $\sim$50% of Class I sources including flat-spectrum remain after distance correction, whereas only $\sim$26% of Class II sources remain. This indicates that in a region at larger distance, the YSO census is likely biased to an earlier class so that $N_{\rm ClassII}/N_{\rm ClassI}$ becomes lower. We do not correct distance for Vul OB1 since it is at a similar distance (2.3 kpc) to IRDC G53.2. We summarize the newly computed $N_{\rm ClassII}/N_{\rm ClassI}$ for each region after correcting classification and distance in Table 5. Number ratio of Class II to Class I in a star-forming region is sensitive to both classification scheme and distance, and each factor changes the ratio by a factor of two. We do not make any correction for the IRDC-associated YSOs from Bhavya et al. (2013) because their catalog is not available. The IRDCs in their samples are mostly farther away (3–6 kpc) than IRDC G53.2, so $N_{\rm ClassII}/N_{\rm ClassI}$ will become higher by a factor of two if assuming the distance of 1.7 kpc. On the other hand, they classified the sources based on $\alpha_{\rm IRAC}$, so the use of $\alpha_{2-24\mu m}$will make $N_{\rm ClassII}/N_{\rm ClassI}$ lower by a factor of two. Therefore, their corrected $N_{\rm ClassII}/N_{\rm ClassI}$ may not be very different from the uncorrected ones.

Under the same classification criteria and assuming the same distance, all of the compared regions and IRDC G53.2 show similar $N_{\rm ClassII}/N_{\rm ClassI}$, which indicates that they are similar in age or at a similar evolutionary stage. We note that there may be more Class I objects in IRDC G53.2 that are too deeply embedded to be detected even in 24 μm because of high column density of the

central part of the IRDC. Such sources are, however, beyond the scope of this study, and further investigation including longer wavebands will be helpful to search for them.

6.2.2. Comparison with Other IRDCs

Star formation activity in IRDCs has mostly been studied on core (10^{-2}–10^{-1} pc) or clump (10^{-1}–10^{0} pc) scales, so a direct comparison of the stellar population in different IRDCs, as in Section 6.2.1, is difficult. Some studies, however, address the issues on protostars detected at 24 μm in the vicinity of IRDCs and their association. The 24 μm point-source detection is one of the signs to trace star formation activity in IRDC clumps and related to their evolutionary phase. IRDC clumps are suggested to evolve from a quiescent clump to an active/red clump with an intermediate clump in between. As clumps evolve, they become warmer and show tracers of star formation such as embedded 24 μm point sources or H_2O/CH_3OH maser emission (Chambers et al. 2009; Battersby et al. 2010). A large number of YSO candidates detected in 24 μm in IRDC G53.2, with the associated "green fuzzies (extended 4.5 μm enhancement)" and H_2O/CH_3OH masers previously found (e.g., Chambers et al. 2009), indicates that stars are actively forming in IRDC G53.2 and IRDC G53.2 is likely at a later evolutionary stage among IRDCs.

Ragan et al. (2009) investigated stellar content around 11 IRDCs at 2.4–4.9 kpc using *Spitzer* data. They found many Class II and a few Class I objects, but only ∼10% of them were associated with the IRDC clumps identified by the absorption in 8 μm. From the clump mass function, which is shallower than the Salpeter mass function, and a lack of association between the clumps and mid-IR sources, the authors suggested that IRDCs are the precursors to stellar clusters in an early phase of fragmentation. In the IRDC G011.11-0.12, Henning et al. (2010) found ∼20 embedded cores in a diverse mass range (1–240 $M_\odot$), half of which were associated with the 24 μm detection. From large spacings between the cores, well in excess of the Jeans length in the IRDC (see Section 6.3.2 below), the authors also concluded that IRDC cores are at an early stage in protostar formation with a capability of forming massive stars and clusters. These IRDC clumps in the early phase of fragmentation (Henning et al. 2010; Ragan et al. 2009) are very weakly associated with 24 μm point sources with lower surface density of sources in mid-IR compared to IRDC G53.2. This again implies a more evolved status for IRDC G53.2. The cores in the IRDC G011.11-0.12 or in the IRDCs in Ragan et al. (2009) may represent an earlier stage than that seen in IRDC G53.2, before active star formation has turned on. Future studies on stellar mass function in IRDC G53.2 or on physical properties of the clumps harboring bright 24 μm sources will be helpful for further comparison between IRDC G53.2 and other IRDCs at various evolutionary stages.

6.2.3. Age Estimation Using Analytic Model

Myers (2012) developed an analytic model of protostar mass and luminosity evolution in clusters that provides estimates of cluster age, protostar birthrate, accretion rate, and mean accretion time, under the assumptions of constant protostar birthrate, core-clump accretion, and equally likely accretion stopping. Based on the model, the age of a star-forming cluster can be described as $t \simeq \bar{a}/[\nu(1+\nu^2/2(1-\nu))]$ (Equation (38) of Myers 2012), where $\bar{a}$ is the accretion timescale and ν is the fraction of protostars among total YSOs in the cluster. From this, Myers (2012) estimated the ages and birthrates of 31 nearby clusters and complexes using the observed numbers of protostars and Class II YSOs assuming the accretion timescale of 0.17 Myr and the equal numbers of Class II and Class III sources (see Section 5 of Myers 2012 for details). In the above equation, the term $\nu^2/[2(1-\nu)]$ becomes negligible as ν decreases, so that the equation can be approximated by $N_{\rm ClassII}/N_{\rm ClassI}$ and the age of a star-forming cluster as $t \simeq 2\bar{a}(N_{\rm ClassII}/N_{\rm ClassI} + 1/2)$. We apply this relation to IRDC G53.2, assuming the same accretion timescale of 0.17 Myr, and the estimated age of IRDC G53.2 is ∼0.5 Myr. This age may be highly uncertain because of several assumptions used in the model, particularly the accretion timescale, which varies from 0.12 to 0.4–0.5 Myr (Myers 2012 and references therein). The age of the nearby star-forming clusters in Gutermuth et al. (2009) using $N_{\rm ClassII}/N_{\rm ClassI}$ after correcting for classification and distance (Section 6.2.1) ranges from 0.2 to 1.1 Myr, with a median of 0.5 Myr. This is comparable to the estimated age of IRDC G53.2.

6.3. Spatial Distribution of the YSO Candidates

6.3.1. Distribution of the YSO Candidates in the Molecular Cloud and Far-IR Emission

As Figure 1 shows, bright mid-IR sources in IRDC G53.2 are located along dark filaments in 24 μm. Based on the classification in Section 4, we examine the spatial distribution of the YSO candidates in IRDC G53.2 in a relation to the associated CO molecular cloud and far-IR emission. Figure 9 shows the distribution of the YSO candidates in each class on a ^{13}CO column density map we construct from the GRS ^{13}CO $J = 1$–0 image integrated at $v = 15$–30 km s^{-1} (Section 2). Overall, the YSO candidates are dispersed within the boundary of IRDC G53.2 as drawn by the magenta contour, though they are also more concentrated where the ^{13}CO column density is higher.

Column density of the molecular cloud shows a good correlation with far-IR continuum emission as well. For comparison, intensity contours from the *Herschel*[12] SPIRE (Griffin et al. 2010) 500 μm image[13] with levels of 3, 5, and 8 Jy beam^{-1} are presented in white on the column density map in

[12] *Herschel* is an ESA space observatory with science instruments provided by European-led Principal Investigator consortia and with important participation from NASA.

[13] Level 2 image retrieved from Herschel Science Archive (http://www.cosmos.esa.int/web/herschel/science-archive)

Figure 9, and three peak positions (one in the eastern and two in the western part of the IRDC) in both column density and 500 μm intensity are spatially coincident. We note that there is far-IR emission outside of the IRDC G53.2 boundary to the north and west of the IRDC. This emission is probably not related to IRDC G53.2 but, rather, to foreground emission from CO clouds at another velocity observed along the same line of sight (see Figure 2).

In Figure 9, Class I objects are clustered within the 500 μm contours, particularly higher intensity levels, whereas Class II or III objects are rather randomly distributed. We examine the degree of clustering by comparing the numbers of objects in each class within the 500 μm contours. Table 6 presents the numbers of the YSO candidates in each class within the 500 μm contours of 8, 5, 3, and 2 Jy beam^{-1}. If we compare Class I and II objects, $\gtrsim$40% of the Class I objects are distributed within 5 Jy beam^{-1}, where only $\sim$22% of the Class II objects are placed. This indicates that Class I objects or YSOs in earlier classes are more concentrated where the 500 μm intensity is higher, although flat-spectrum objects are more widely distributed. Clustering of Class I YSOs at high-extinction regions or the regions with high column density is often shown in other star-forming regions as well (e.g., Gutermuth et al. 2009; Myers 2012 and references therein; Chavarría et al. 2014).

We also compare $N_{\rm ClassII}/N_{\rm ClassI}$ in each level of the 500 μm contours. Flat-spectrum objects are again included with the Class I objects. If Class I objects are concentrated in a denser region surrounded by more evolved YSOs, $N_{\rm ClassII}/N_{\rm ClassI}$ will increase as larger regions are considered, from the densest region to the outer region, and there will be a gradient in the ratios. Myers (2012), using the protostar fraction, investigated age structures in well-studied star-forming regions, Serpens north/south clusters and the CrA cluster, and found that there are local age variations from 0.3 to 0.9 Myr. In Table 6 we present $N_{\rm ClassII}/N_{\rm ClassI}$ in the 500 μm contours of each level in IRDC G53.2. The central region with higher (>8 Jy beam^{-1}) 500 μm intensity or higher ^{13}CO column density shows smaller $N_{\rm ClassII}/N_{\rm ClassI}$ of 0.6, compared to 0.9 for the whole IRDC. The difference is small, and a local gradient among the intensity levels is hardly seen, likely owing to a small sample size. Compared to the area of the IRDC, the number of YSO candidates is rather small, which makes a statistical comparison of the number of sources in each contour zone difficult. However, we still see that Class I objects are likely concentrated along the denser filament in IRDC G53.2. If we apply the relation between $N_{\rm ClassII}/N_{\rm ClassI}$ and age we derive in Section 6.2.3 from Myers (2012), it gives $\sim$0.2 Myr of age variation in IRDC G53.2

On the other hand, several recent studies have shown clustering of Class I YSOs along filamentary structures or pre- and protostellar core formation along IRDCs, many of which are likely massive (Teixeira et al. 2006; Henning et al. 2010; Jackson et al. 2010; Bhavya et al. 2013). Therefore, spatial concentration of earlier-class objects along the bright emission in the *Herschel* image supports star formation in very early phases occurring in IRDC G53.2 and gives a possibility that a fraction of the early-phase YSOs are massive. Detailed modeling of the objects using a full SED including longer wavebands in the future will be necessary to investigate physical characteristics of YSOs forming in IRDC G53.2.

6.3.2. Spacings of the YSO Candidates

In analysis of the spatial distribution of YSOs in star-forming regions, an average spacing between sources is often used to investigate the fragmentation processes in relation with the Jeans fragmentation and the subsequent dynamical evolution of the stars since YSOs are expected to move away from their birth sites as they evolve (Teixeira et al. 2006; Kumar et al. 2007; Winston et al. 2007; Gutermuth et al. 2009). One indicator to examine spacings between YSOs is a nearest-neighbor distance, which is the projected distance to the nearest YSO, often noted as NN2 distance (Gutermuth et al. 2009). In the study of the "Spokes" cluster in the young cluster NGC 2264, Teixeira et al. (2006) found a clear peak in their histogram of NN2 distances and suggested that the peak indicates the Jeans fragmentation of dense, dusty filaments. A peak at small spacings with a relatively long tail of large spacings in NN2 distance histograms is shown in young, nearby, star-forming clusters as well, and when the histograms show a pronounced peak and tail, the cumulative distributions have a steep inner slope and a shallow outer slope (e.g., Figure 2 of Gutermuth et al. 2009).

The histogram of the NN2 distances of the YSO candidates in IRDC G53.2 also shows a well-defined peak, as presented in Figure 10(a), with a median value of 0.2 pc. The dashed line in the figure marks the $5''$ (or 0.04 pc at 1.7 kpc) boundary below which the source confusion becomes significant (Gutermuth et al. 2009), which means that the most frequent spacing ($\sim$0.2 pc) is not an effect of resolution. As Gutermuth et al. (2009) pointed out, the cumulative distribution of the NN2 distance has a steep slope at small spacings and a shallow slope at large spacings. In Figure 10(b), we compare the NN2 distances of each YSO class. We include flat-spectrum objects in Class I, and they still show a clear peak at $\sim$0.2 pc. The NN2 distances of Class II objects also have a peak, but not as sharp as that of Class I, and the NN2 distances of Class III are rather broadly distributed at larger spacings. We present the median of the NN2 distances of each class in Table 7. The NN2 distance histograms of each class indicate that Class I objects are more highly clustered with smaller spacings (0.2 pc in median) than later classes (0.4 and 0.7 pc in median for Class II and Class III, respectively), and their normalized cumulative distributions presented in Figure 10(c) more clearly show this. In Figure 10(c), the cumulative distribution of Class I has much steeper slope at small spacings than the other two classes. The NN2 distances that contain 70% of the sources in each class are 0.3, 0.5, and 0.7 pc for Class I, II, and III, respectively (see Table 7).

We perform a Kolmogorov−Smirnov (K-S) test to examine the probability that the parent distributions of each class are the same. Table 8 presents the K-S probabilities of the normalized cumulative distributions of the NN2 distances between each class. The results show $< 1\%$ chance of similarity between any of two classes, implying that Class I objects are typically closer to their nearest neighbors than Class II or III objects. Such a tendency was more obviously shown in a study on the Serpens cloud core, where the median NN2 distances of Class I, flat-spectrum, Class II, and Class III are 0.024, 0.079, 0.097, and 0.132 pc, respectively (Winston et al. 2007). An increase in the median distance between YSOs for more evolved sources/classes supports the idea

that stars are born in a dense region and dispersed away from the birth site as they evolve, and the smaller spacing of Class I objects in IRDC G53.2 indicates that such a process is occurring in IRDC G53.2 as well.

On the other hand, the median NN2 distance of IRDC G53.2 is about a factor of two larger than that of nearby star-forming clusters. For comparison, the mean value of the median NN2 distances of 36 nearby, young clusters in Gutermuth et al. (2009) is 0.07 pc. The relatively larger spacing of the sources in IRDC G53.2 is likely due to its larger distance. As discussed in Section 6.2.1, there is a selection effect in the sources in IRDC G53.2 from distance so that the NN2 distances of the sources in the IRDC can be biased to higher values by the smaller number of the sources compared to the whole area (and hence a lower surface density of sources). Although the mean of the median NN2 distances of the clusters in Gutermuth et al. (2009) is 0.07 pc, the median NN2 distances of the individual clusters are spread up to ∼0.4 pc, and they in general show a good correlation with the distance to the clusters as we present in Figure 11. In this plot, although there are a few outliers that are not easily explained, the NN2 distance of the sources in IRDC G53.2, lying on the tendency of the relation between distance and NN2 distance, is not particularly large when one takes into account its distance.

In the Spokes cluster at a distance of 800 pc, Teixeira et al. (2006) found a typical separation of ∼0.1 pc for protostars distributed along its dusty filaments. This length scale is in very good agreement with the Jeans length in the cluster, so they suggested thermal fragmentation of the dense filamentary material. The NN2 distance of the Spokes cluster is also smaller than that of IRDC G53.2. The assumption that the Spokes cluster is at the same distance as IRDC G53.2 does not change the result because Teixeira et al. (2006) only used the bright 24 μm sources that are detectable at 1.7 kpc. However, the surface density of sources in the Spokes cluster is higher owing to its smaller area than IRDC G53.2, and we need to analyze the NN2 distance in a subregion with high source surface density in IRDC G53.2 to make a suitable comparison. There are three subregions where the YSO candidates are concentrated in Figure 9 that are consistent with the 3 Jy beam^{-1} of the 500 μm contour, as well as dark filaments in 24 μm. We derive the NN2 distances of one of the subregions marked with an arrow "A" in Figure 9, where the YSO candidates are located along the dark filament in 24 μm (see Figure 1). The number of the YSO candidates in the region A is 41, and the median NN2 distance is ∼0.1 pc, resulting in a similar length scale to that of the Spokes cluster.

The NN2 distance in the region A is also comparable with the Jeans length, given as $\lambda_{\rm J} = (\pi c_s^2/G\rho_0)^{1/2} = 0.21\ {\rm pc}(T/10{\rm K})^{1/2} \times (n_{\rm H_2}/10^4{\rm cm}^{-3})^{-1/2}$ (McKee & Ostriker 2007; Winston et al. 2007) for initial temperature ∼20 K and density $\sim 10^5{\rm cm}^{-3}$, which are typical values in IRDCs (Pillai et al. 2006; Rathborne et al. 2006; Ragan et al. 2011). Comparing with the mean core separation of ∼0.9 pc in the IRDC G011.11-0.12 (Henning et al. 2010), this indicates that IRDC G53.2, in which Jeans fragmentation is likely dominant, is more evolved than the IRDC G011.11-0.12. More detailed investigation on this subregion using far-IR data and/or molecular line maps such as HNC (1–0) (e.g., Jackson et al. 2010) will be useful to explore the fragmentation and star

formation processes occurring in dense filamentary IRDCs.

7. Summary and Conclusions

We present star formation activity in IRDC G53.2, which is a long, filamentary IRDC at Galactic coordinates $(l, b) \sim (53°.2, 0°.0)$ using *Spitzer* mid-IR data. We summarize our results and give conclusions below.

1. We found that IRDC G53.2 previously identified as several separate IRDCs in the mid-IR images coincides precisely with a CO cloud at $v \sim 23$ km s^{-1}. This gives a kinematic distance of 1.7 kpc to IRDC G53.2, and the cloud mass determined from CO emission is $\sim 10^5 M_\odot$.

2. We made a PSC of IRDC G53.2 based on the photometry of *Spitzer* MIPSGAL 24 μm data. The finalized catalog after merging with the GLIMPSE Catalog contains 373 sources in total, including four sources saturated in the MIPS 24 μm image but listed in the *MSX* PSC.

3. Based on the spectral index defined in the range 2–24 μm, we classified the sources in the catalog. Since IRDC G53.2 is located in the Galactic plane, there is negligible extragalactic contamination but substantial field star contamination, so that we accounted for the field star contamination by control field analysis. The census of the YSO candidates in the IRDC, if we remove the expected field star contamination, is determined as follows: 77 Class I (25%), 63 flat-spectrum (21%), 129 Class II (42%), 33 Class III (11%), and 6 No Class (∼1%) without enough data points to determine spectral index.

4. We compared the classification of YSO candidates based on different classification schemes such as spectral index, mid-IR colors, and the wavelength range used. Different classifications using different criteria generally agree well, but flat-spectrum sources show high uncertainty with an ambiguity between Class I and Class II. High extinction toward IRDC G53.2 may also affect classification of flat-spectrum sources, but the effect on the overall statistics is not likely significant.

5. We compared the census of the YSO candidates in IRDC G53.2 with those of other well-studied star-forming regions. A similar fraction of Class I objects in IRDC G53.2 and other regions indicates that IRDC G53.2 is similar in age or at a similar evolutionary stage to the nearby star-forming regions. On the other hand, the comparison of stellar population to other IRDCs shows that IRDC G53.2, with strong association with mid-IR stellar sources, is at a later evolutionary status among IRDCs.

6. Spatial distribution of the YSO candidates in IRDC G53.2 shows a good correlation with ^{13}CO column density and far-IR emission, and earlier-class objects tend to be more clustered where ^{13}CO column density is higher. Overall, the median distance between the YSO candidates and their nearest neighbors is 0.2 pc, and earlier-class objects have smaller spacing, which indicates that YSOs disperse away from their birth sites as they evolve. In a small, denser region with high surface density of sources, the median nearest-neighbor distance is ∼0.1 pc, which is comparable

to the Jeans length scale.

Characterizing star formation activity in IRDC G53.2 based on the census of YSO candidates presented in this study provides an insight on the star-forming process occurring in IRDCs, particularly in an aspect of an associated molecular cloud rather than in an individual IRDC. We found YSOs in various evolutionary phases, and our results suggest that IRDC G53.2 is an active star-forming region where Jeans fragmentation is likely dominant. Spatial distribution of the YSO candidates, which has a correlation with far-IR emission and the objects only detected in the 24 μm but not in the IRAC bands, may imply the existence of much younger YSOs embedded in the IRDC. Further studies on full SEDs of YSO candidates including longer wavebands to derive mass and luminosity distribution of YSOs in IRDC G53.2 will help to investigate in more detail the nature and star formation properties of IRDCs.

This publication makes use of molecular line data from the Boston University−FCRAO Galactic Ring Survey (GRS). The GRS is a joint project of Boston University and Five College Radio Astronomy Observatory, funded by the National Science Foundation under grants AST-9800334, AST-0098562, and AST-0100793. This publication makes use of data products from the Two Micron All Sky Survey, which is a joint project of the University of Massachusetts and the Infrared Processing and Analysis Center/California Institute of Technology, funded by the National Aeronautics and Space Administration and the National Science Foundation. This work is based on observations made with the Spitzer Space Telescope, which is operated by the Jet Propulsion Laboratory, California Institute of Technology, under a contract with NASA. This research has made use of the SIMBAD database, operated at CDS, Strasbourg, France. This work was supported by NRF(National Research Foundation of Korea) Grant funded by the Korean Government (NRF-2012-Fostering Core Leaders of the Future Basic Science Program). B.-C.K. was supported by the National Research Foundation of Korea (NRF) grant funded by the Korea Government (MSIP) (No. 2012R1A4A1028713).

REFERENCES

Aguirre, J. E., Ginsburg, A. G., Dunham, M. K., et al. 2011, ApJS, 192, 4

André, P. 2002, EAS Publications Series, 3, 1

Battersby, C., Bally, J., Jackson, J. M., et al. 2010, ApJ, 721, 222

Benjamin, R. A., Churchwell, E., Babler, B. L., et al. 2003, PASP, 115, 953

Bhavya, B., Subramaniam, A., & Kuriakose, V. C. 2013, MNRAS, 435, 663

Billot, N., Noriega-Crespo, A., Carey, S., et al. 2010, ApJ, 712, 797

Butler, M. J., & Tan, J. C. 2012, ApJ, 754, 5

Calvet, N., Hartmann, L., Kenyon, S. J., & Whitney, B. A. 1994, ApJ, 434, 330

Carey, S. J., Clark, F. O., Egan, M. P., et al. 1998, ApJ, 508, 721

Carey, S. J., Feldman, P. A., Redman, R. O., et al. 2000, ApJ, 543, L157

Carey, S. J., Noriega-Crespo, A., Mizuno, D. R., et al. 2009, PASP, 121, 76

Chambers, E. T., Jackson, J. M., Rathborne, J. M., & Simon, R. 2009, ApJS, 181, 360

Chapman, N. L., Mundy, L. G., Lai, S.-P., & Evans, N. J., II 2009, ApJ, 690, 496

Chavarría, L., Allen, L., Brunt, C., et al. 2014, MNRAS, 439, 3719

Clemens, D. P., Sanders, D. B., Scoville, N. Z., & Solomon, P. M. 1986, ApJS, 60, 297

Crapsi, A., van Dishoeck, E. F., Hogerheijde, M. R., Pontoppidan, K. M., & Dullemond, C. P. 2008, A&A, 486, 245

Egan, M. P., Price, S. D., Kraemer, K. E., et al. 2003, VizieR Online Data Catalog, 5114, 0

Egan, M. P., Shipman, R. F., Price, S. D., et al. 1998, ApJ, 494, L199

Evans, N. J., II, Allen, L. E., Blake, G. A., et al. 2003, PASP, 115, 965

Evans, N. J., II, Dunham, M. M., Jørgensen, J. K., et al. 2009, ApJS, 181, 321

Flaherty, K. M., Pipher, J. L., Megeath, S. T., et al. 2007, ApJ, 663, 1069

Greene, T. P., Wilking, B. A., Andre, P., Young, E. T., & Lada, C. J. 1994, ApJ, 434, 614

Griffin, M. J., Abergel, A., Abreu, A., et al. 2010, A&A, 518, L3

Gutermuth, R. A., Megeath, S. T., Myers, P. C., et al. 2009, ApJS, 184, 18

Gutermuth, R. A., Myers, P. C., Megeath, S. T., et al. 2008, ApJ, 674, 336

Henning, T., Linz, H., Krause, O., et al. 2010, A&A, 518, L95

Heyer, M., Krawczyk, C., Duval, J., & Jackson, J. M. 2009, ApJ, 699, 1092

Jackson, J. M., Finn, S. C., Chambers, E. T., Rathborne, J. M., & Simon, R. 2010, ApJ, 719, L185

Jackson, J. M., Rathborne, J. M., Shah, R. Y., et al. 2006, ApJS, 163, 145

Kumar, M. S. N., Davis, C. J., Grave, J. M. C., Ferreira, B., & Froebrich, D. 2007, MNRAS, 374, 54

Lada, C. J. 1987, Star Forming Regions, 115, 1

Lada, C. J., Muench, A. A., Luhman, K. L., et al. 2006, AJ, 131, 1574

Lada, C. J., & Wilking, B. A. 1984, ApJ, 287, 610

Liu, X.-L., Wang, J.-J., & Xu, J.-L. 2014, MNRAS, 443, 2264

Lonsdale, C. J., Smith, H. E., Rowan-Robinson, M., et al. 2003, PASP, 115, 897

Mamajek, E. E. 2009, American Institute of Physics Conference Series, 1158, 3

McKee, C. F., & Ostriker, E. C. 2007, ARA&A, 45, 565

Milam, S. N., Savage, C., Brewster, M. A., Ziurys, L. M., & Wyckoff, S. 2005, ApJ, 634, 1126

Myers, P. C. 2012, ApJ, 752, 9

Peretto, N., & Fuller, G. A. 2009, A&A, 505, 405

Peretto, N., & Fuller, G. A. 2010, ApJ, 723, 555

Pillai, T., Wyrowski, F., Carey, S. J., & Menten, K. M. 2006, A&A, 450, 569

Pineda, J. L., Goldsmith, P. F., Chapman, N., et al. 2010, ApJ, 721, 686

Ragan, S. E., Bergin, E. A., & Gutermuth, R. A. 2009, ApJ, 698, 324

Ragan, S. E., Bergin, E. A., & Wilner, D. 2011, ApJ, 736, 163

Ragan, S. E., Henning, T., Tackenberg, J., et al. 2014, A&A, 568, AA73

Rathborne, J. M., Jackson, J. M., & Simon, R. 2006, ApJ, 641, 389

Rebull, L. M., Guieu, S., Stauffer, J. R., et al. 2011, ApJS, 193, 25

Reid, M. J., Menten, K. M., Zheng, X. W., et al. 2009, ApJ, 700, 137

Robitaille, T. P., Whitney, B. A., Indebetouw, R., Wood, K., & Denzmore, P. 2006, ApJS, 167, 256

Rohlfs, K., & Wilson, T. L. 2000, Tools of radio astronomy / K. Rohlfs, T.L. Wilson. New York : Springer, 2000. (Astronomy and astrophysics library, ISSN0941-7834)

Roman-Duval, J., Jackson, J. M., Heyer, M., Rathborne, J., & Simon, R. 2010, ApJ, 723, 492

Sanders, D. B., Clemens, D. P., Scoville, N. Z., & Solomon, P. M. 1986, ApJS, 60, 1

Simon, R., Jackson, J. M., Rathborne, J. M., & Chambers, E. T. 2006a, ApJ, 639, 227

Simon, R., Rathborne, J. M., Shah, R. Y., Jackson, J. M., & Chambers, E. T. 2006b, ApJ, 653, 1325

Skrutskie, M. F., Cutri, R. M., Stiening, R., et al. 2006, AJ, 131, 1163

Teixeira, P. S., Lada, C. J., Young, E. T., et al. 2006, ApJ, 636, L45

van der Wiel, M. H. D., & Shipman, R. F. 2008, A&A, 490, 655

Winston, E., Megeath, S. T., Wolk, S. J., et al. 2007, ApJ, 669, 493

Ybarra, J. E., Lada, E. A., Román-Zúñiga, C. G., et al. 2013, ApJ, 769, 140

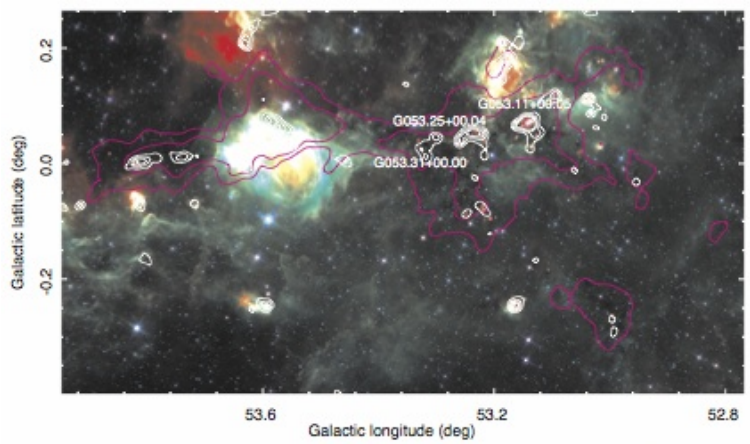

Fig. 1.— Three-color image of IRDC G53.2 produced from *Spitzer* IRAC 5.8 μm (B), IRAC 8.0 μm (G), and MIPS 24 μm (R) images. The magenta contours are from the GRS ^{13}CO $J = 1$–0 integrated intensity map at $v = 15$–30 km s^{-1} (see Section 2 and Figure 2). The outermost contour level, which defines the boundary of IRDC G53.2, is $\int T_{mb} dv = 6.3$ K km s^{-1} or the mean antenna temperature $\bar{T}_A (= 0.48 \bar{T}_{mb}) = 0.2$ K. The Bolocam Galactic Plane Survey (Aguirre et al. 2011) 1.2 mm contours are also overlaid in white. The previously identified three IRDCs in the MSXDC catalog (Simon et al. 2006a) are marked.

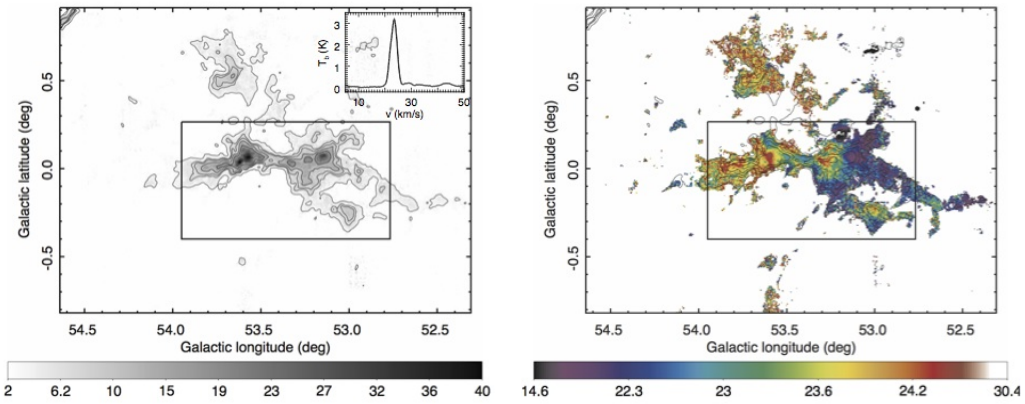

Fig. 2.— Left: ^{13}CO $J = 1$–0 integrated intensity map of the IRDC G53.2 region. The velocity range is from $v_{\rm LSR} = +15$ to $+30$ km s^{-1}. The scale bar shows the integrated intensity scale, and the contour levels are drawn at $\int T_{mb} dv$ =3.1, 6.3, 7.9, 11.0, and 15.7 K km s^{-1} (or the mean antenna temperature $\bar{T}_A (= 0.48 \bar{T}_{mb})$ =0.1, 0.2, 0.25, 0.35, and 0.5 K). The inset shows the average spectrum of the cloud, and the square box marks the area of Figure 1. Right: Mean velocity of the ^{13}CO gas in IRDC G53.2. The velocity scale (km s^{-1}) is given by the scale bar at the bottom. The contour levels of the integrated intensity are overlaid.

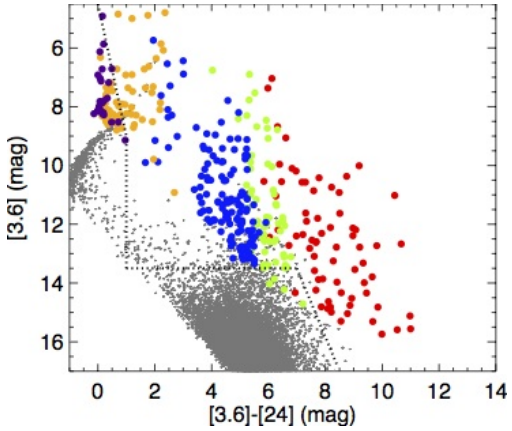

Fig. 3.— [3.6] vs. [3.6]–[24] plot for objects in the IRDC G53.2 region and SWIRE (Lonsdale et al. 2003) ELAIS N-1. Red, green, blue, yellow, and purple circles indicate Class I, flat-spectrum, Class II, Class III, and photospheric sources, respectively. Gray dots are SWIRE ELAIS N-1 samples. The dotted line divides the regions occupied mostly by SWIRE-type contaminants (galaxies and diskless stars) and where YSOs (Rebull et al. 2011).

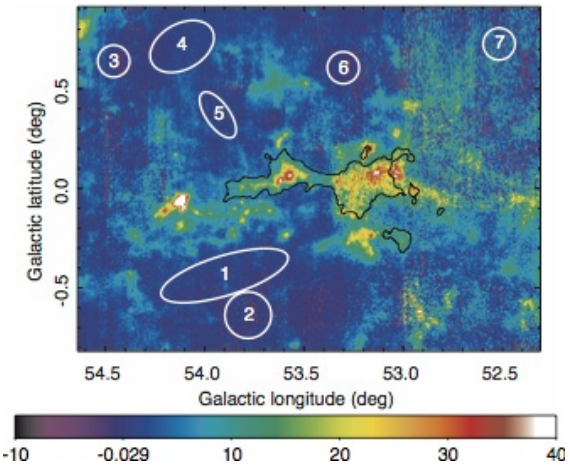

Fig. 4.— Same as the left panel of Figure 2, but the integration has been done over the entire velocity range of the GRS survey, i.e., $v_{\rm LSR} = -5$ to $+85$ km s^{-1}. Seven white ellipses and circles with numbers are control fields, and the black contour shows the boundary of IRDC G53.2. The scale bar indicates the integrated intensity scale.

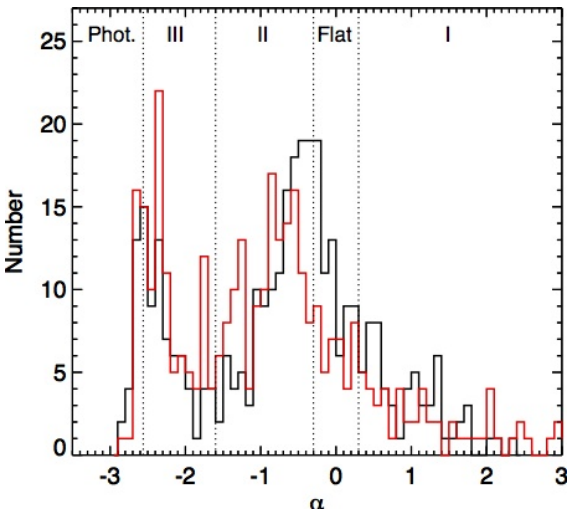

Fig. 5.— Histogram of spectral indices of the point sources in IRDC G53.2. Black and red lines are spectral indices computed by least-squares linear fitting in the range 2–24 μm and only using the IRAC bands, respectively. Dotted lines divide the regions for each class.

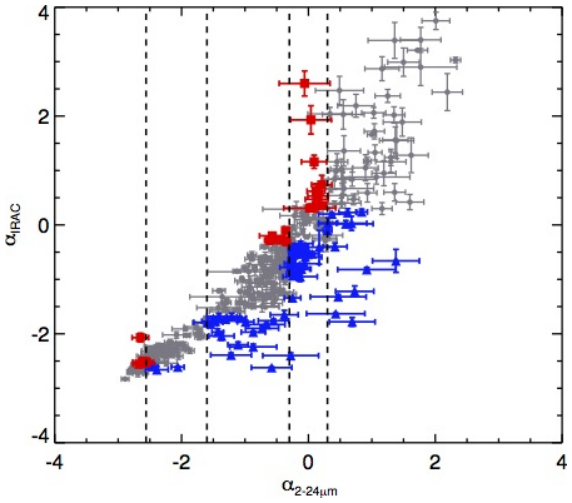

Fig. 6.— Comparison between spectral indices of the point sources in IRDC G53.2 computed using 2–24 μm ($\alpha_{2-24\mu\mathrm{m}}$) and using only the IRAC bands (α_{IRAC}). Gray circles are the objects whose classes from the both spectral indices are the same. Blue triangles are the objects whose class from α_{IRAC} is later than that from $\alpha_{2-24\mu\mathrm{m}}$, and red squares are the objects whose class from α_{IRAC} is earlier than that from $\alpha_{2-24\mu\mathrm{m}}$. Dashed lines divide the regions for each class based on $\alpha_{2-24\mu\mathrm{m}}$.

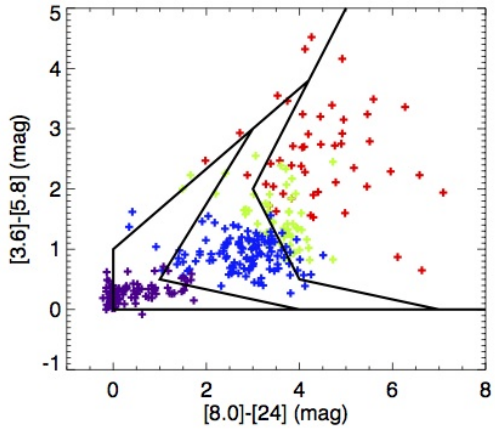

Fig. 7.— Color-color diagram using the IRAC bands at 3.6, 5.8, 8.0 μm and the MIPS 24 μm. Red, green, blue, and purple crosses represent Class I, flat-spectrum, Class II, and Class III/photospheric sources in IRDC G53.2, respectively, classified based on the spectral index $\alpha_{2-24\mu m}$. Black solid lines divide the areas filled by Stage I, II, and III sources from right to left, adopted from Figure 18 of Robitaille et al. (2006).

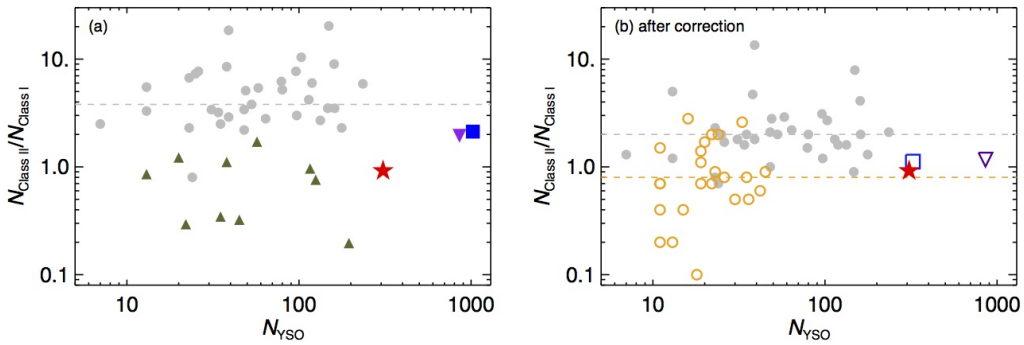

Fig. 8.— (a) Number ratios of Class II to Class I objects vs. the number of YSOs of IRDC G53.2 (filled red star) and in other star-forming regions. Filled gray circles: 36 nearby star-forming clusters (Gutermuth et al. 2009) with their median value of 3.7 marked by a gray dashed line; filled green triangles: filamentary structures in the inner Galactic region (Bhavya et al. 2013); filled blue square: the c2d clouds (Evans et al. 2009); filled purple downward-pointing triangle: Vul OB1 (Billot et al. 2010). (b) Number ratios of Class II to Class I objects after correcting for different classification schemes and distances (Section 6.2.1). Filled gray circles: the clusters in Gutermuth et al. (2009) adapted to the $\alpha_{2-24\mu m}$-based classification scheme with their median value of 2.0 marked by a grey-dashed line; open orange circles: the clusters in Gutermuth et al. (2009) after scaling to the distance of IRDC G53.2 with the median value of 0.8 marked by an orange dashed line; open blue square: the c2d clouds after distance correction; open purple downward-pointing triangle: Vul OB1 based on the $\alpha_{2-24\mu m}$-based classification.

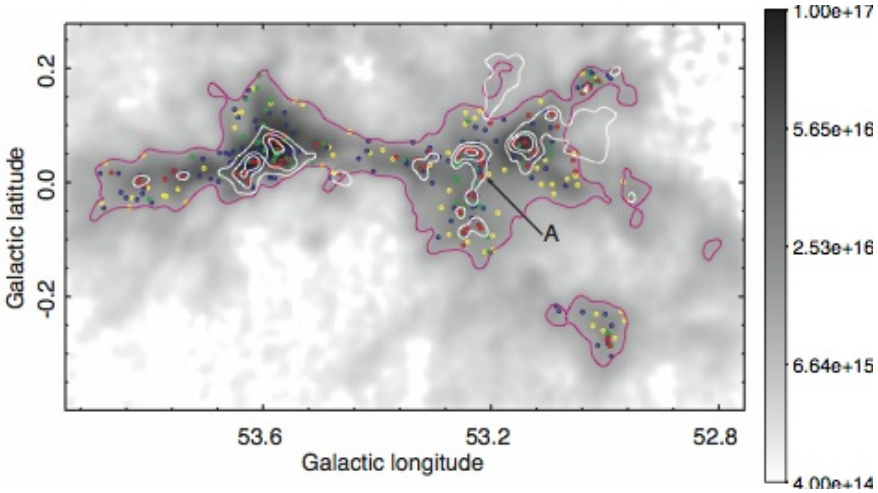

Fig. 9.— Spatial distribution of the YSO candidates in IRDC G53.2 on a column density map constructed from the GRS ^{13}CO J = 1–0 image integrated at v = 15–30 km s^{-1} (Section 2). The map is smoothed, and the scale bar indicates ^{13}CO column density of the image in cm^{-2}. The magenta contour presents the boundary of IRDC G53.2, and white contours are the *Herschel* SPIRE 500 μm intensity contours of 3, 5, and 8 Jy beam^{-1}. Red, green, blue, and yellow symbols present Class I, flat-spectrum, Class II, and Class III objects, respectively. For the arrow marked with "A", see Section 6.3.2.

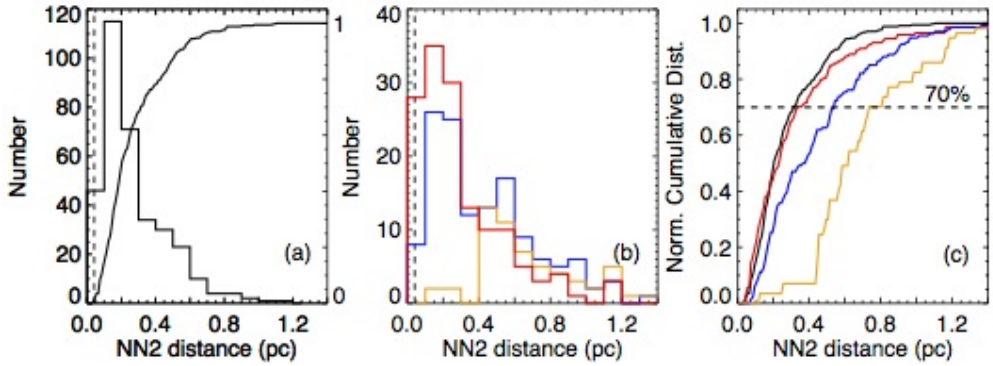

Fig. 10.— (a) Histogram of NN2 distance of IRDC G53.2 with a bin size of 0.1 pc. The dashed line marks the 5″ boundary below which source confusion becomes significant. The normalized cumulative distribution is overplotted. (b) Histograms of NN2 distance for each class of YSO of IRDC G53.2. Red, blue, and orange histograms present (Class I + flat-spectrum), Class II, and Class III objects, respectively. The bin size is 0.1 pc as well. (c) Normalized cumulative distribution of the NN2 distances of each YSO class. Colors are the same as those used in (b), and the black line presents all of the YSO candidates.

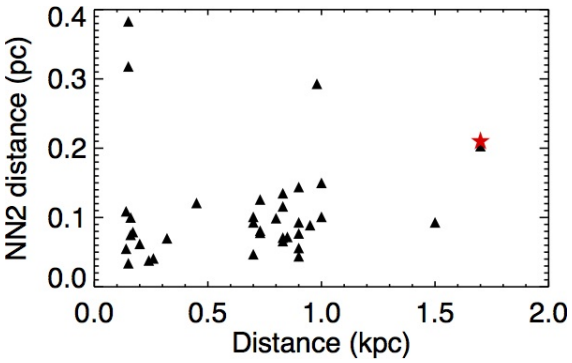

Fig. 11.— Median NN2 distances of 36 nearby, young, star-forming clusters from Gutermuth et al. (2009) vs. their distances (black triangles). The median NN2 distance of IRDC G53.2 is marked with a red star.

Table 1. Parameters of IRDC G53.2

Parameter	IRDC G53.2
Center (l, b)	$\sim (53°.21, -0°.086)$
Angular Size	$\sim 1°.5 \times 0°.7$
Linear Size	45 pc $\times$ 21 pc
$v_{/rmcenter}$	$+22.9 \pm 1.0$ (km s^{-1})
$\Delta v_{rmwidth}$	1.7 ± 0.5 (km s^{-1})
Kinematic distance	1.7 (kpc)
Mass	6.2×10^{4a} , 1×10^{5b} ($M_\odot$)
Surface density	0.076^a , 0.033^b (g cm^{-2})

[a]The boundary of IRDC G53.2 for the analysis of the star formation activity in mid-IR (the ^{13}CO integrated intensity contour at $\int T_{mb} dv = 6.3$ K km s^{-1}).

[b]The cloud boundary accounting for its low-density envelope (at $\int T_{mb} dv = 2.1$ K km s^{-1}). See Section 2.

Table 2. Point-source Catalog of IRDC G53.2

No	R.A. (J2000)	Decl. (J2000)	J	H	K_s	[3.6]	[4.5]	[5.8]	[8.0]	[24]	α [a]	Class [b]
1	19:30:19.59	18:18:17.21	11.84 ± 0.022	11.11 ± 0.022	10.72 ± 0.021	10.57 ± 0.156	10.26 ± 0.181	...	...	3.27 ± 0.044	...	I[d]
2	19:30:22.95	18:20:27.92	...	...	13.83 ± 0.076	10.01 ± 0.214	7.39 ± 0.159	5.69 ± 0.026	4.94 ± 0.025	0.82 ± 0.061	1.77 ± 0.57	I
3	19:30:22.14	18:20:46.43	14.83 ± 0.049	12.71 ± 0.034	11.46 ± 0.031	9.67 ± 0.061	8.84 ± 0.063	8.23 ± 0.060	7.80 ± 0.183	5.62 ± 0.046	-0.74 ± 0.19	II
4	19:30:14.05	18:18:22.50	12.91 ± 0.025	11.33 ± 0.022	10.27 ± 0.018	9.09 ± 0.039	8.65 ± 0.047	8.15 ± 0.036	7.30 ± 0.029	4.16 ± 0.045	-0.55 ± 0.05	II[a]
5	19:30:17.10	18:19:43.00	11.97 ± 0.025	...	...	6.44 ± 0.063	...	5.64 ± 0.036	5.21 ± 0.025	3.44 ± 0.045	-1.30 ± 0.08	II[a]
6	19:30:25.17	18:23:24.18	11.61 ± 0.020	8.91 ± 0.027	7.43 ± 0.022	5.74 ± 0.062	...	5.09 ± 0.026	4.84 ± 0.027	3.79 ± 0.044	-1.58 ± 0.23	II[a]
7	19:30:12.58	18:18:13.46	...	13.95 ± 0.040	10.54 ± 0.020	6.76 ± 0.032	6.20 ± 0.103	4.76 ± 0.027	4.22 ± 0.026	2.73 ± 0.044	-0.19 ± 0.53	Flat[a]
8	19:30:20.61	18:21:34.20	...	14.33 ± 0.057	13.09 ± 0.043	11.18 ± 0.090	10.68 ± 0.077	10.01 ± 0.115	...	6.30 ± 0.044	-0.37 ± 0.12	II
9	19:30:23.02	18:22:45.34	12.80 ± 0.023	11.43 ± 0.022	10.54 ± 0.020	9.34 ± 0.042	8.97 ± 0.045	8.74 ± 0.049	8.33 ± 0.035	5.64 ± 0.045	-1.08 ± 0.09	II
10	19:30:13.25	18:18:50.76	14.23 ± 0.032	11.51 ± 0.024	9.66 ± 0.018	7.77 ± 0.115	7.07 ± 0.070	6.49 ± 0.033	5.75 ± 0.028	2.45 ± 0.044	-0.22 ± 0.09	Flat
11	19:30:15.97	18:19:56.21	15.98 ± 0.080	14.70 ± 0.064	14.05 ± 0.071	12.55 ± 0.059	11.93 ± 0.078	11.13 ± 0.113	10.31 ± 0.085	6.57 ± 0.047	-0.03 ± 0.03	Flat[a]
12	19:30:11.89	18:18:35.86	...	...	14.69 ± 0.107	10.10 ± 0.049	8.72 ± 0.046	7.63 ± 0.036	6.85 ± 0.029	3.27 ± 0.045	1.07 ± 0.53	I
13	19:30:13.95	18:19:53.90	...	...	11.15 ± 0.038	9.83 ± 0.046	9.29 ± 0.049	8.97 ± 0.051	8.52 ± 0.104	5.65 ± 0.045	-0.86 ± 0.08	II
14	19:30:14.63	18:21:05.22	14.31 ± 0.035	13.00 ± 0.029	12.40 ± 0.027	11.16 ± 0.081	10.79 ± 0.074	10.36 ± 0.336	...	5.59 ± 0.044	-0.25 ± 0.13	Flat
15	19:30:10.20	18:19:08.22	...	...	...	12.35 ± 0.051	10.98 ± 0.059	9.96 ± 0.045	8.97 ± 0.103	5.14 ± 0.045	0.44 ± 0.12	I
16	19:30:13.53	18:20:50.50	16.81 ± 0.169	14.90 ± 0.072	13.82 ± 0.049	12.59 ± 0.069	11.71 ± 0.068	10.68 ± 0.110	9.90 ± 0.253	6.54 ± 0.045	-0.05 ± 0.07	Flat
17	19:30:11.24	18:19:59.92	...	...	...	13.79 ± 0.142	11.28 ± 0.074	10.30 ± 0.080	9.73 ± 0.251	4.14 ± 0.044	1.39 ± 0.27	I
18	19:30:09.01	18:21:41.98	14.05 ± 0.030	12.73 ± 0.023	12.03 ± 0.025	11.19 ± 0.042	10.71 ± 0.048	10.16 ± 0.048	9.24 ± 0.029	6.48 ± 0.046	-0.72 ± 0.06	II
19	19:30:13.43	18:23:51.94	10.24 ± 0.020	8.21 ± 0.017	7.31 ± 0.016	6.72 ± 0.025	6.80 ± 0.043	6.45 ± 0.022	6.30 ± 0.024	5.09 ± 0.045	-2.07 ± 0.05	III[a]
20	19:30:06.40	18:21:23.44	...	14.60 ± 0.065	13.38 ± 0.056	12.02 ± 0.042	11.61 ± 0.075	11.16 ± 0.084	10.16 ± 0.059	6.43 ± 0.045	-0.24 ± 0.10	Flat
21	19:30:07.55	18:24:21.85	10.66 ± 0.020	8.41 ± 0.020	7.35 ± 0.018	6.63 ± 0.037	6.76 ± 0.050	6.36 ± 0.035	6.15 ± 0.027	4.84 ± 0.044	-1.96 ± 0.06	III[a] |
22	19:30:06.37	18:24:47.66	12.39 ± 0.024	11.47 ± 0.026	10.87 ± 0.021	9.65 ± 0.079	9.38 ± 0.081	9.01 ± 0.049	7.93 ± 0.024	4.47 ± 0.045	-0.44 ± 0.12	I[a]
23	19:29:55.45	18:21:54.86	10.93 ± 0.022	10.59 ± 0.030	10.40 ± 0.029	10.04 ± 0.050	9.74 ± 0.060	7.81 ± 0.037	5.58 ± 0.047	3.92 ± 0.044	-0.06 ± 0.40	Flat
24	19:29:54.24	18:24:06.80	8.86 ± 0.024	6.80 ± 0.026	5.82 ± 0.018	5.00 ± 0.096	5.18 ± 0.067	4.81 ± 0.030	4.63 ± 0.027	3.80 ± 0.045	-2.16 ± 0.08	III[a] |
25	19:29:49.40	18:22:32.63	9.70 ± 0.022	7.94 ± 0.016	7.20 ± 0.020	6.72 ± 0.057	6.94 ± 0.043	6.62 ± 0.031	6.62 ± 0.026	6.57 ± 0.045	-2.66 ± 0.09	Phot[a]
26	19:29:47.99	18:24:11.95	13.99 ± 0.025	12.93 ± 0.023	12.40 ± 0.022	11.90 ± 0.054	11.53 ± 0.086	10.72 ± 0.173	...	5.40 ± 0.044	-0.05 ± 0.26	Flat[a]
27	19:30:39.06	18:29:14.06	10.02 ± 0.021	8.33 ± 0.022	7.57 ± 0.026	7.18 ± 0.038	7.30 ± 0.044	7.01 ± 0.037	6.94 ± 0.040	6.80 ± 0.046	-2.60 ± 0.07	Phot
28	19:30:24.82	18:22:58.69	14.97 ± 0.036	13.71 ± 0.032	13.03 ± 0.032	11.87 ± 0.046	11.46 ± 0.073	11.12 ± 0.103	10.49 ± 0.082	7.77 ± 0.048	-0.91 ± 0.05	II[a]
29	19:30:14.75	18:18:43.88	...	...	14.49 ± 0.090	12.72 ± 0.068	12.22 ± 0.084	11.51 ± 0.117	...	7.34 ± 0.048	-0.19 ± 0.07	Flat
30	19:30:26.55	18:23:59.21	12.12 ± 0.023	11.55 ± 0.023	11.26 ± 0.021	11.07 ± 0.030	11.10 ± 0.058	10.65 ± 0.065	...	7.49 ± 0.045	-1.37 ± 0.20	II
31	19:30:11.51	18:17:42.86	14.90 ± 0.042	13.27 ± 0.029	12.06 ± 0.022	10.36 ± 0.041	9.92 ± 0.054	9.54 ± 0.048	8.86 ± 0.056	6.72 ± 0.046	-0.93 ± 0.12	II
32	19:30:16.90	18:20:38.98	16.08 ± 0.085	14.28 ± 0.047	13.39 ± 0.040	12.19 ± 0.088	11.82 ± 0.113	11.16 ± 0.199	10.11 ± 0.250	6.75 ± 0.045	-0.32 ± 0.08	II
33	19:30:10.99	18:17:51.40	15.66 ± 0.073	13.93 ± 0.038	12.95 ± 0.034	11.59 ± 0.069	11.27 ± 0.069	10.70 ± 0.091	9.97 ± 0.107	6.88 ± 0.045	-0.60 ± 0.06	II
34	19:30:19.78	18:22:06.82	15.43 ± 0.053	14.11 ± 0.039	13.66 ± 0.062	13.15 ± 0.073	12.52 ± 0.093	12.03 ± 0.203	10.96 ± 0.171	7.71 ± 0.047	-0.52 ± 0.14	II
35	19:30:12.99	18:19:56.78	11.88 ± 0.025	11.47 ± 0.028	11.24 ± 0.032	11.39 ± 0.059	11.36 ± 0.084	11.06 ± 0.150	...	6.35 ± 0.045	-0.87 ± 0.37	II
36	19:30:06.23	18:18:29.95	...	15.36 ± 0.116	14.47 ± 0.087	12.94 ± 0.072	12.24 ± 0.135	11.72 ± 0.113	10.65 ± 0.069	7.54 ± 0.046	-0.25 ± 0.04	Flat
37	19:30:15.11	18:22:36.48	15.89 ± 0.076	14.92 ± 0.079	14.30 ± 0.091	13.39 ± 0.088	13.02 ± 0.142	12.19 ± 0.214	11.24 ± 0.210	7.57 ± 0.048	-0.25 ± 0.13	Flat
38	19:30:06.17	18:18:55.40	...	...	...	14.99 ± 0.152	13.84 ± 0.143	12.64 ± 0.329	...	6.78 ± 0.047	1.00 ± 0.07	I
39	19:30:07.48	18:19:39.90	16.57 ± 0.130	14.46 ± 0.045	13.06 ± 0.033	11.23 ± 0.049	10.69 ± 0.061	10.12 ± 0.049	9.72 ± 0.137	7.01 ± 0.046	-0.68 ± 0.13	II
40	19:30:06.33	18:22:19.20	15.04 ± 0.042	13.66 ± 0.032	12.88 ± 0.030	11.84 ± 0.096	11.58 ± 0.087	11.40 ± 0.132	10.88 ± 0.061	7.76 ± 0.048	-0.99 ± 0.13	II
41	19:30:08.65	18:24:04.72	13.93 ± 0.025	12.88 ± 0.020	12.32 ± 0.022	11.34 ± 0.064	11.06 ± 0.060	10.82 ± 0.067	10.13 ± 0.034	6.95 ± 0.045	-0.86 ± 0.13	II
42	19:30:00.48	18:21:24.16	14.87 ± 0.052	13.36 ± 0.040	12.49 ± 0.031	11.27 ± 0.078	10.79 ± 0.098	10.69 ± 0.069	10.10 ± 0.046	7.62 ± 0.047	-1.09 ± 0.08	II
43	19:30:02.33	18:22:18.52	13.06 ± 0.024	10.23 ± 0.022	8.96 ± 0.017	8.15 ± 0.040	8.29 ± 0.046	7.96 ± 0.039	7.94 ± 0.026	8.16 ± 0.048	-2.61 ± 0.16	Phot
44	19:29:57.00	18:19:59.84	15.37 ± 0.051	14.30 ± 0.052	13.62 ± 0.043	12.28 ± 0.067	11.68 ± 0.074	11.15 ± 0.073	10.37 ± 0.046	7.35 ± 0.045	-0.51 ± 0.03	II
45	19:30:05.96	18:24:00.22	11.92 ± 0.025	9.86 ± 0.028	8.95 ± 0.022	8.38 ± 0.039	8.19 ± 0.106	8.19 ± 0.023	8.14 ± 0.028	7.67 ± 0.046	-2.45 ± 0.08	III
46	19:29:59.78	18:21:50.15	...	...	...	12.94 ± 0.068	12.30 ± 0.100	11.69 ± 0.136	10.85 ± 0.062	7.07 ± 0.045	-0.07 ± 0.06	Flat
47	19:29:56.36	18:21:45.94	12.11 ± 0.025	10.72 ± 0.039	10.13 ± 0.028	9.79 ± 0.076	9.65 ± 0.105	9.64 ± 0.050	9.56 ± 0.039	7.83 ± 0.047	-2.06 ± 0.10	III
48	19:30:00.05	18:24:13.97	...	...	...	14.22 ± 0.135	13.03 ± 0.134	11.83 ± 0.138	11.27 ± 0.079	7.67 ± 0.046	0.12 ± 0.14	Flat
49	19:29:59.55	18:24:23.08	15.91 ± 0.064	14.30 ± 0.041	13.44 ± 0.037	12.80 ± 0.064	12.48 ± 0.116	12.15 ± 0.164	11.63 ± 0.095	7.67 ± 0.046	-0.68 ± 0.22	II
50	19:29:56.00	18:24:28.04	14.16 ± 0.043	13.45 ± 0.035	13.08 ± 0.037	12.75 ± 0.063	12.56 ± 0.107	12.07 ± 0.124	11.24 ± 0.095	7.69 ± 0.046	-0.76 ± 0.22	II
51	19:29:53.34	18:23:46.64	...	...	...	13.39 ± 0.084	12.47 ± 0.103	11.55 ± 0.078	10.62 ± 0.068	6.80 ± 0.044	0.23 ± 0.04	Flat

Table 2—Continued

No	R.A. (J2000)	Decl. (J2000)	J	H	K_s	[3.6]	[4.5]	[5.8]	[8.0]	[24]	α [a]	Class [b]
52	19:31:02.65	18:29:46.36	11.70 ± 0.020	9.23 ± 0.022	7.84 ± 0.024	6.36 ± 0.039	6.15 ± 0.047	5.72 ± 0.029	5.49 ± 0.023	4.31 ± 0.045	-1.62 ± 0.17	III[a]
53	19:31:03.88	18:30:20.41	13.55 ± 0.024	12.01 ± 0.025	11.13 ± 0.021	9.88 ± 0.075	9.37 ± 0.070	8.79 ± 0.040	7.98 ± 0.033	5.53 ± 0.045	-0.75 ± 0.04	II
54	19:30:54.73	18:26:44.74	8.89 ± 0.025	7.10 ± 0.026	6.18 ± 0.021	5.86 ± 0.064	···	5.34 ± 0.031	5.17 ± 0.025	3.64 ± 0.044	-1.92 ± 0.05	III[a]
55	19:30:54.96	18:27:00.11	11.80 ± 0.021	9.42 ± 0.023	8.23 ± 0.020	7.52 ± 0.055	7.56 ± 0.058	7.22 ± 0.034	7.09 ± 0.032	5.62 ± 0.044	-1.94 ± 0.06	III[a]
56	19:30:56.34	18:29:12.55	15.23 ± 0.044	13.70 ± 0.036	12.57 ± 0.022	11.26 ± 0.087	10.77 ± 0.064	10.26 ± 0.056	9.63 ± 0.034	6.66 ± 0.045	-0.66 ± 0.04	II
57	19:30:37.39	18:21:39.64	9.02 ± 0.022	7.39 ± 0.034	6.69 ± 0.020	6.71 ± 0.052	···	6.09 ± 0.031	6.08 ± 0.026	6.22 ± 0.045	-2.65 ± 0.13	Phot[a]
58	19:30:54.69	18:29:18.38	···	···	14.22 ± 0.079	11.04 ± 0.055	9.92 ± 0.054	9.00 ± 0.041	8.22 ± 0.028	4.78 ± 0.044	0.52 ± 0.31	I
59	19:30:55.42	18:29:57.95	···	···	···	11.02 ± 0.047	8.60 ± 0.045	6.86 ± 0.030	5.50 ± 0.027	0.58 ± 0.044	1.77 ± 0.32	I
60	19:30:31.35	18:19:53.47	12.59 ± 0.023	11.72 ± 0.023	11.20 ± 0.022	10.86 ± 0.150	···	10.27 ± 0.111	···	3.27 ± 0.044	···	I[d]
61	19:30:31.50	18:21:24.16	···	14.96 ± 0.126	12.71 ± 0.050	9.96 ± 0.071	9.06 ± 0.062	8.40 ± 0.048	7.81 ± 0.071	3.57 ± 0.044	0.42 ± 0.19	I
62	19:30:48.34	18:27:39.82	···	···	···	13.86 ± 0.076	11.57 ± 0.066	10.31 ± 0.052	9.48 ± 0.068	5.95 ± 0.045	0.55 ± 0.33	I
63	19:30:24.49	18:17:37.39	14.06 ± 0.023	12.95 ± 0.020	12.20 ± 0.018	10.99 ± 0.058	10.60 ± 0.057	10.17 ± 0.064	9.61 ± 0.083	6.62 ± 0.046	-0.79 ± 0.06	II
64	19:30:34.85	18:22:39.61	···	···	14.83 ± 0.110	12.53 ± 0.060	11.33 ± 0.053	10.61 ± 0.102	10.20 ± 0.263	6.28 ± 0.045	0.25 ± 0.19	Flat
65	19:30:29.49	18:20:32.71	···	···	···	12.78 ± 0.064	11.02 ± 0.076	9.63 ± 0.058	8.52 ± 0.036	3.57 ± 0.045	1.35 ± 0.17	I
66	19:30:57.28	18:32:56.94	···	···	···	12.39 ± 0.089	10.72 ± 0.050	9.19 ± 0.040	7.87 ± 0.026	3.42 ± 0.044	1.25 ± 0.20	I
67	19:30:28.72	18:20:35.88	···	···	···	11.62 ± 0.057	10.04 ± 0.082	8.93 ± 0.042	8.37 ± 0.063	4.31 ± 0.045	0.41 ± 0.17	I
68	19:30:43.41	18:27:17.86	···	···	···	12.54 ± 0.074	10.88 ± 0.061	9.84 ± 0.056	9.11 ± 0.053	5.01 ± 0.045	0.52 ± 0.17	I
69	19:30:27.00	18:20:12.16	12.43 ± 0.030	11.71 ± 0.038	11.40 ± 0.034	11.14 ± 0.085	10.97 ± 0.065	10.60 ± 0.158	···	5.89 ± 0.044	-0.66 ± 0.29	II
70	19:30:27.64	18:20:28.14	13.72 ± 0.023	12.55 ± 0.023	11.79 ± 0.021	10.50 ± 0.051	10.21 ± 0.073	9.82 ± 0.062	9.34 ± 0.089	6.53 ± 0.045	-0.94 ± 0.08	II
71	19:30:24.43	18:19:39.00	13.80 ± 0.027	12.16 ± 0.024	10.96 ± 0.020	9.42 ± 0.044	8.88 ± 0.051	8.55 ± 0.036	8.04 ± 0.046	5.04 ± 0.044	-0.71 ± 0.09	II
72	19:30:20.69	18:18:28.19	12.14 ± 0.025	11.27 ± 0.026	10.78 ± 0.026	10.42 ± 0.223	10.14 ± 0.155	9.62 ± 0.320	···	2.64 ± 0.044	0.47 ± 0.44	I
73	19:30:26.89	18:21:19.04	16.25 ± 0.097	14.16 ± 0.041	12.87 ± 0.032	11.49 ± 0.056	10.89 ± 0.062	10.23 ± 0.107	···	6.25 ± 0.044	-0.36 ± 0.02	II
74	19:30:15.89	18:16:39.83	12.69 ± 0.023	12.07 ± 0.022	11.73 ± 0.021	10.98 ± 0.105	10.94 ± 0.096	8.72 ± 0.085	7.19 ± 0.117	4.78 ± 0.045	0.04 ± 0.32	Flat
75	19:30:21.61	18:20:01.72	···	···	···	13.09 ± 0.201	12.72 ± 0.307	···	···	5.48 ± 0.044	···	I[d]
76	19:30:24.82	18:21:11.48	14.16 ± 0.026	12.27 ± 0.020	11.01 ± 0.018	9.44 ± 0.041	8.93 ± 0.052	8.37 ± 0.046	7.33 ± 0.062	4.21 ± 0.044	-0.31 ± 0.04	II
77	19:30:20.10	18:19:08.51	11.68 ± 0.022	10.71 ± 0.023	10.10 ± 0.021	9.01 ± 0.046	8.71 ± 0.045	8.16 ± 0.020	7.62 ± 0.038	6.22 ± 0.045	-1.41 ± 0.10	II
78	19:30:18.17	18:18:36.14	15.04 ± 0.047	12.91 ± 0.026	11.48 ± 0.020	9.66 ± 0.044	8.98 ± 0.046	8.24 ± 0.035	7.35 ± 0.037	4.25 ± 0.045	-0.17 ± 0.09	Flat
79	19:30:16.48	18:17:54.96	···	···	···	12.11 ± 0.075	10.07 ± 0.047	8.65 ± 0.036	7.67 ± 0.049	3.93 ± 0.045	0.75 ± 0.29	I
80	19:30:23.47	18:20:56.40	···	14.01 ± 0.101	12.41 ± 0.064	10.67 ± 0.045	9.90 ± 0.039	9.40 ± 0.059	8.78 ± 0.049	5.44 ± 0.044	-0.29 ± 0.09	Flat
81	19:30:22.78	18:20:50.75	14.31 ± 0.037	11.82 ± 0.031	10.27 ± 0.025	9.46 ± 0.080	8.81 ± 0.110	8.09 ± 0.075	7.35 ± 0.043	4.66 ± 0.045	-0.69 ± 0.05	II
82	19:30:14.63	18:17:22.42	···	···	···	14.82 ± 0.256	13.24 ± 0.106	11.66 ± 0.176	···	4.97 ± 0.045	1.72 ± 0.16	I
83	19:30:21.75	18:20:53.05	15.88 ± 0.078	12.32 ± 0.026	10.65 ± 0.021	9.43 ± 0.064	9.41 ± 0.126	9.03 ± 0.084	8.92 ± 0.311	5.70 ± 0.044	-1.11 ± 0.16	II
84	19:30:16.24	18:18:37.98	···	15.32 ± 0.090	12.82 ± 0.025	11.01 ± 0.050	10.54 ± 0.071	10.01 ± 0.069	···	5.64 ± 0.046	-0.19 ± 0.08	Flat
85	19:30:43.59	18:30:55.73	9.95 ± 0.020	8.70 ± 0.026	7.98 ± 0.020	7.36 ± 0.033	7.12 ± 0.033	6.94 ± 0.035	6.82 ± 0.019	6.30 ± 0.045	-2.27 ± 0.09	III
86	19:31:12.55	18:31:53.72	···	14.97 ± 0.070	14.07 ± 0.067	12.75 ± 0.053	12.15 ± 0.139	11.72 ± 0.110	10.48 ± 0.054	7.48 ± 0.047	-0.35 ± 0.06	II
87	19:31:06.93	18:29:34.12	12.54 ± 0.021	10.13 ± 0.022	9.03 ± 0.017	8.23 ± 0.030	8.39 ± 0.042	8.01 ± 0.027	7.92 ± 0.031	7.22 ± 0.047	-2.24 ± 0.09	III
88	19:31:11.48	18:32:13.34	11.33 ± 0.021	9.04 ± 0.022	7.96 ± 0.020	7.34 ± 0.047	7.45 ± 0.052	7.12 ± 0.035	7.06 ± 0.029	7.05 ± 0.046	-2.56 ± 0.12	III
89	19:30:52.81	18:24:32.72	12.07 ± 0.023	9.83 ± 0.025	8.77 ± 0.020	7.91 ± 0.087	7.92 ± 0.069	7.65 ± 0.034	7.56 ± 0.026	7.08 ± 0.045	-2.29 ± 0.11	III
90	19:31:02.20	18:29:15.29	···	···	···	11.90 ± 0.041	11.55 ± 0.076	11.12 ± 0.096	10.53 ± 0.053	7.93 ± 0.048	-0.98 ± 0.05	II
91	19:30:59.53	18:28:06.42	···	···	···	13.86 ± 0.071	13.74 ± 0.135	12.23 ± 0.202	10.98 ± 0.051	7.65 ± 0.045	0.21 ± 0.16	Flat
92	19:31:02.89	18:31:05.66	15.95 ± 0.082	14.16 ± 0.045	13.20 ± 0.039	12.54 ± 0.058	12.14 ± 0.057	11.65 ± 0.075	10.63 ± 0.036	7.10 ± 0.045	-0.49 ± 0.16	II
93	19:30:49.51	18:25:59.88	12.97 ± 0.021	10.29 ± 0.022	9.03 ± 0.018	8.26 ± 0.041	8.29 ± 0.040	7.95 ± 0.037	7.90 ± 0.025	7.46 ± 0.046	-2.33 ± 0.11	III
94	19:30:32.81	18:19:04.01	···	14.60 ± 0.055	13.45 ± 0.040	11.98 ± 0.051	11.43 ± 0.083	11.12 ± 0.082	···	6.98 ± 0.045	-0.44 ± 0.07	II
95	19:30:55.35	18:28:49.73	11.50 ± 0.020	9.23 ± 0.022	8.18 ± 0.017	7.49 ± 0.043	7.63 ± 0.046	7.31 ± 0.030	7.27 ± 0.026	7.14 ± 0.045	-2.52 ± 0.11	III
96	19:30:32.25	18:18:50.36	14.80 ± 0.049	13.64 ± 0.048	13.09 ± 0.045	12.47 ± 0.062	12.23 ± 0.080	···	···	7.78 ± 0.050	···	No Class
97	19:30:32.18	18:19:22.51	15.57 ± 0.065	13.89 ± 0.041	12.96 ± 0.038	11.95 ± 0.074	11.77 ± 0.102	11.18 ± 0.090	···	6.88 ± 0.045	-0.52 ± 0.14	II
98	19:30:37.82	18:22:38.46	15.59 ± 0.063	14.63 ± 0.061	14.25 ± 0.071	12.91 ± 0.104	12.27 ± 0.106	11.69 ± 0.144	10.98 ± 0.131	7.88 ± 0.048	-0.47 ± 0.03	II
99	19:30:38.41	18:23:29.22	···	···	14.33 ± 0.075	12.97 ± 0.068	12.50 ± 0.093	11.68 ± 0.099	11.02 ± 0.088	7.64 ± 0.047	-0.34 ± 0.04	II
100	19:30:25.20	18:18:05.58	16.00 ± 0.087	14.35 ± 0.068	13.48 ± 0.057	11.92 ± 0.045	11.37 ± 0.072	10.81 ± 0.087	10.01 ± 0.071	7.58 ± 0.048	-0.67 ± 0.09	II
101	19:30:24.43	18:17:58.38	···	···	11.74 ± 0.032	11.17 ± 0.077	11.00 ± 0.099	10.71 ± 0.104	···	6.64 ± 0.045	-0.87 ± 0.19	II
102	19:30:52.48	18:30:10.15	···	14.99 ± 0.070	13.24 ± 0.036	11.93 ± 0.054	11.24 ± 0.069	10.78 ± 0.065	9.97 ± 0.050	7.98 ± 0.049	-0.89 ± 0.11	II

Table 2—Continued

No	R.A. (J2000)	Decl. (J2000)	J	H	K_s	[3.6]	[4.5]	[5.8]	[8.0]	[24]	α [a]	Class [b]
103	19:31:00.01	18:33:58.93	14.36 ± 0.029	13.12 ± 0.027	12.48 ± 0.025	11.27 ± 0.051	10.54 ± 0.056	9.93 ± 0.032	9.14 ± 0.025	6.74 ± 0.045	-0.69 ± 0.07	II
104	19:30:56.03	18:32:16.66	···	···	···	12.97 ± 0.061	12.36 ± 0.089	11.67 ± 0.061	10.59 ± 0.049	7.70 ± 0.045	-0.36 ± 0.05	II
105	19:30:33.15	18:22:32.66	14.43 ± 0.029	13.41 ± 0.029	13.10 ± 0.034	12.66 ± 0.083	12.70 ± 0.099	···	···	7.10 ± 0.045	···	No Class
106	19:30:41.60	18:26:12.41	13.13 ± 0.021	12.04 ± 0.022	11.40 ± 0.018	10.50 ± 0.042	10.03 ± 0.046	9.62 ± 0.051	9.08 ± 0.036	6.64 ± 0.046	-1.08 ± 0.02	II
107	19:30:43.19	18:27:14.76	···	15.01 ± 0.064	11.45 ± 0.017	9.15 ± 0.036	8.70 ± 0.050	8.11 ± 0.038	8.06 ± 0.034	7.14 ± 0.073	-1.42 ± 0.34	II
108	19:30:24.97	18:19:55.24	15.67 ± 0.065	14.10 ± 0.036	13.17 ± 0.032	12.04 ± 0.069	11.58 ± 0.079	11.12 ± 0.148	···	7.02 ± 0.045	-0.52 ± 0.07	II
109	19:30:15.32	18:17:44.88	15.16 ± 0.050	13.50 ± 0.043	12.40 ± 0.036	11.35 ± 0.057	11.09 ± 0.099	10.49 ± 0.113	10.07 ± 0.188	6.40 ± 0.045	-0.62 ± 0.14	II
110	19:30:54.68	18:34:01.06	11.70 ± 0.020	9.93 ± 0.022	8.99 ± 0.018	8.26 ± 0.053	8.20 ± 0.053	7.92 ± 0.035	7.69 ± 0.044	7.08 ± 0.044	-2.18 ± 0.09	III
111	19:30:28.12	18:22:29.75	···	13.81 ± 0.048	13.01 ± 0.044	11.99 ± 0.056	11.42 ± 0.058	11.19 ± 0.118	10.31 ± 0.275	7.35 ± 0.046	-0.73 ± 0.07	II
112	19:30:26.90	18:22:12.58	···	14.54 ± 0.052	13.33 ± 0.033	11.60 ± 0.055	11.06 ± 0.066	10.62 ± 0.072	10.21 ± 0.104	6.60 ± 0.045	-0.42 ± 0.12	II
113	19:30:14.21	18:17:11.40	···	···	14.64 ± 0.097	12.51 ± 0.090	11.69 ± 0.082	11.26 ± 0.130	10.44 ± 0.241	7.09 ± 0.046	-0.11 ± 0.13	Flat
114	19:30:18.72	18:19:19.49	···	14.78 ± 0.057	13.61 ± 0.041	12.42 ± 0.076	11.88 ± 0.097	11.15 ± 0.107	10.52 ± 0.164	6.89 ± 0.051	-0.32 ± 0.07	II
115	19:30:44.54	18:30:39.67	9.69 ± 0.020	8.12 ± 0.017	7.46 ± 0.018	7.13 ± 0.053	7.28 ± 0.035	7.06 ± 0.035	6.98 ± 0.019	7.02 ± 0.046	-2.73 ± 0.07	Phot
116	19:30:14.29	18:17:31.74	···	···	14.52 ± 0.089	12.91 ± 0.072	12.17 ± 0.079	11.27 ± 0.136	10.61 ± 0.122	7.70 ± 0.051	-0.30 ± 0.10	Flat
117	19:30:33.77	18:26:19.64	···	···	···	13.39 ± 0.077	12.93 ± 0.134	12.46 ± 0.156	11.37 ± 0.071	7.51 ± 0.046	-0.01 ± 0.10	Flat
118	19:30:20.70	18:20:38.83	12.89 ± 0.037	11.45 ± 0.032	10.33 ± 0.018	8.92 ± 0.039	8.58 ± 0.054	8.07 ± 0.036	7.51 ± 0.071	5.09 ± 0.044	-0.94 ± 0.07	II
119	19:30:13.56	18:17:24.40	···	14.11 ± 0.065	···	11.31 ± 0.058	10.72 ± 0.075	10.11 ± 0.121	···	6.36 ± 0.045	-0.49 ± 0.02	II
120	19:31:00.30	18:27:43.31	15.65 ± 0.061	14.43 ± 0.052	13.72 ± 0.050	13.15 ± 0.067	12.95 ± 0.110	12.58 ± 0.186	···	7.84 ± 0.046	-0.55 ± 0.24	II
121	19:30:58.79	18:29:01.61	15.94 ± 0.075	14.77 ± 0.061	14.05 ± 0.056	13.22 ± 0.074	12.96 ± 0.122	12.65 ± 0.229	11.80 ± 0.150	7.71 ± 0.046	-0.45 ± 0.22	II
122	19:30:39.75	18:24:41.83	···	···	14.70 ± 0.105	12.64 ± 0.055	11.99 ± 0.077	11.47 ± 0.085	10.82 ± 0.056	7.91 ± 0.047	-0.40 ± 0.14	II
123	19:30:35.81	18:24:39.28	14.69 ± 0.034	11.18 ± 0.022	9.48 ± 0.018	8.37 ± 0.047	8.42 ± 0.045	8.01 ± 0.036	7.99 ± 0.027	8.14 ± 0.048	-2.42 ± 0.21	III
124	19:30:32.41	18:25:13.04	···	···	14.40 ± 0.086	12.89 ± 0.099	12.36 ± 0.103	11.77 ± 0.098	11.28 ± 0.091	7.81 ± 0.046	-0.43 ± 0.08	II
125	19:30:14.77	18:18:34.38	···	···	14.12 ± 0.063	12.39 ± 0.092	11.83 ± 0.163	10.79 ± 0.207	···	6.77 ± 0.045	-0.10 ± 0.09	Flat
126	19:30:53.73	18:30:13.43	···	···	14.67 ± 0.102	12.59 ± 0.076	11.72 ± 0.104	11.72 ± 0.114	11.02 ± 0.070	4.91 ± 0.045	0.73 ± 0.30	I
127	19:30:10.47	18:17:08.81	16.17 ± 0.103	13.69 ± 0.038	12.48 ± 0.027	11.02 ± 0.037	10.43 ± 0.063	9.86 ± 0.061	9.11 ± 0.099	6.00 ± 0.044	-0.44 ± 0.04	II
128	19:30:08.86	18:16:42.31	12.53 ± 0.022	11.33 ± 0.024	10.66 ± 0.021	10.14 ± 0.047	10.11 ± 0.066	10.01 ± 0.115	···	4.89 ± 0.044	-0.58 ± 0.32	II
129	19:30:01.44	18:14:23.60	13.25 ± 0.022	12.56 ± 0.022	12.25 ± 0.020	11.94 ± 0.051	11.85 ± 0.078	11.36 ± 0.115	10.28 ± 0.220	6.03 ± 0.044	-0.40 ± 0.31	II
130	19:30:02.16	18:15:20.30	···	···	···	14.34 ± 0.159	12.99 ± 0.113	12.11 ± 0.136	11.47 ± 0.086	4.89 ± 0.045	1.60 ± 0.22	I
131	19:30:03.24	18:18:09.47	14.73 ± 0.044	12.91 ± 0.032	12.01 ± 0.026	10.51 ± 0.175	9.82 ± 0.048	9.39 ± 0.043	8.71 ± 0.044	6.01 ± 0.045	-0.65 ± 0.08	II
132	19:29:57.22	18:18:12.74	7.71 ± 0.021	6.28 ± 0.018	5.57 ± 0.022	4.92 ± 0.094	···	4.75 ± 0.031	4.72 ± 0.026	4.76 ± 0.045	-2.60 ± 0.14	Phot[a]
133	19:29:50.01	18:18:52.96	8.49 ± 0.025	7.06 ± 0.024	6.53 ± 9.995	6.13 ± 0.045	6.36 ± 0.042	6.11 ± 0.026	6.09 ± 0.025	6.06 ± 0.044	-2.69 ± 0.08	Phot[a]
134	19:29:49.86	18:18:45.22	13.12 ± 0.064	10.62 ± 0.057	9.43 ± 0.026	8.51 ± 0.042	8.55 ± 0.045	8.19 ± 0.033	8.11 ± 0.026	6.59 ± 0.044	-1.87 ± 0.07	III
135	19:29:50.26	18:19:38.32	8.69 ± 0.029	7.24 ± 0.016	···	6.32 ± 0.042	6.53 ± 0.041	6.27 ± 0.035	6.22 ± 0.026	6.23 ± 0.045	-2.39 ± 0.18	III[a]
136	19:30:00.75	18:14:51.58	···	···	14.59 ± 0.106	13.49 ± 0.086	12.96 ± 0.121	12.16 ± 0.181	11.40 ± 0.093	7.65 ± 0.048	-0.21 ± 0.09	Flat
137	19:29:53.05	18:13:31.01	10.98 ± 0.021	9.12 ± 0.020	8.33 ± 0.017	7.86 ± 0.038	7.97 ± 0.046	7.72 ± 0.039	7.66 ± 0.027	7.73 ± 0.047	-2.67 ± 0.10	Phot
138	19:30:12.27	18:12:24.05	15.78 ± 0.071	14.10 ± 0.049	13.15 ± 0.036	12.28 ± 0.063	11.80 ± 0.074	11.12 ± 0.076	10.55 ± 0.076	6.61 ± 0.045	-0.36 ± 0.15	II
139	19:30:09.01	18:11:50.17	···	···	14.69 ± 0.143	10.54 ± 0.046	9.62 ± 0.054	8.82 ± 0.042	8.05 ± 0.039	4.70 ± 0.045	0.59 ± 0.43	I
140	19:30:10.03	18:12:28.01	14.17 ± 0.030	10.84 ± 0.022	9.00 ± 0.017	7.32 ± 0.033	7.06 ± 0.036	6.61 ± 0.032	6.46 ± 0.023	5.38 ± 0.045	-1.62 ± 0.21	III
141	19:30:10.44	18:14:54.60	11.38 ± 0.022	11.13 ± 0.023	10.99 ± 0.018	10.84 ± 0.055	10.86 ± 0.103	10.59 ± 0.072	···	4.67 ± 0.044	-0.28 ± 0.44	Flat
142	19:30:09.58	18:13:52.64	12.77 ± 0.023	10.35 ± 0.020	9.23 ± 0.017	8.44 ± 0.043	8.56 ± 0.041	8.18 ± 0.034	8.14 ± 0.043	6.88 ± 0.045	-2.05 ± 0.07	III
143	19:30:03.14	18:13:24.13	12.62 ± 0.021	10.10 ± 0.022	9.03 ± 0.017	8.25 ± 0.049	8.23 ± 0.042	7.90 ± 0.033	7.84 ± 0.029	7.72 ± 0.047	-2.41 ± 0.14	III
144	19:29:31.19	17:59:51.36	···	···	11.24 ± 0.048	7.37 ± 0.060	6.02 ± 0.067	5.14 ± 0.032	4.27 ± 0.026	1.39 ± 0.044	0.56 ± 0.47	I[a]
145	19:29:32.69	18:00:17.32	15.67 ± 0.060	14.12 ± 0.031	13.34 ± 0.032	12.22 ± 0.063	11.71 ± 0.074	11.05 ± 0.058	10.36 ± 0.061	6.94 ± 0.046	-0.43 ± 0.06	II
146	19:29:33.48	18:00:55.51	11.61 ± 0.024	10.44 ± 0.025	9.64 ± 0.020	8.53 ± 0.036	8.07 ± 0.050	7.58 ± 0.032	6.94 ± 0.031	4.19 ± 0.044	-0.82 ± 0.03	II
147	19:29:12.17	17:51:44.39	···	···	···	12.72 ± 0.052	11.80 ± 0.075	11.19 ± 0.086	10.30 ± 0.095	6.00 ± 0.044	0.30 ± 0.07	I
148	19:29:54.48	18:10:04.12	13.22 ± 0.021	9.96 ± 0.020	8.27 ± 0.018	7.25 ± 0.047	7.35 ± 0.045	6.94 ± 0.034	6.89 ± 0.027	6.81 ± 0.046	-2.37 ± 0.17	III
149	19:29:34.72	18:01:35.36	···	14.91 ± 0.080	13.59 ± 0.047	12.09 ± 0.049	11.21 ± 0.077	10.63 ± 0.056	9.66 ± 0.044	6.24 ± 0.045	-0.09 ± 0.03	Flat
150	19:29:18.81	17:54:44.17	···	···	14.87 ± 0.108	12.40 ± 0.053	11.35 ± 0.061	10.50 ± 0.061	9.72 ± 0.040	5.42 ± 0.045	0.62 ± 0.14	I
151	19:29:41.40	18:04:41.23	···	···	14.63 ± 0.100	12.44 ± 0.078	11.73 ± 0.083	9.97 ± 0.076	8.38 ± 0.093	6.40 ± 0.044	0.34 ± 0.35	I
152	19:29:54.36	18:10:26.94	13.53 ± 0.029	12.16 ± 0.051	11.20 ± 0.035	9.67 ± 0.039	8.94 ± 0.037	8.45 ± 0.034	7.81 ± 0.030	4.41 ± 0.044	-0.34 ± 0.07	II
153	19:29:50.62	18:09:03.13	13.73 ± 0.022	10.17 ± 0.022	8.38 ± 0.017	6.91 ± 0.042	6.85 ± 0.045	6.48 ± 0.024	6.14 ± 0.026	5.71 ± 0.045	-1.94 ± 0.21	III[a]

Table 2—Continued

No	R.A. (J2000)	Decl. (J2000)	J	H	K_s	[3.6]	[4.5]	[5.8]	[8.0]	[24]	α [a]	Class [b]
154	19:29:31.59	18:00:58.90	16.52 ± 0.114	14.51 ± 0.050	13.18 ± 0.031	11.36 ± 0.043	10.36 ± 0.058	9.74 ± 0.051	8.85 ± 0.032	5.08 ± 0.045	0.16 ± 0.07	Flat
155	19:29:39.78	18:04:48.00	12.61 ± 0.023	10.05 ± 0.022	8.56 ± 0.018	7.29 ± 0.049	7.09 ± 0.046	6.65 ± 0.035	6.35 ± 0.025	4.75 ± 0.044	-1.50 ± 0.10	II
156	19:29:31.59	18:01:19.02	···	···	···	13.25 ± 0.068	11.62 ± 0.075	10.90 ± 0.070	10.14 ± 0.045	4.97 ± 0.045	0.93 ± 0.15	I
157	19:29:14.08	17:53:42.79	···	14.05 ± 0.043	11.71 ± 0.021	8.41 ± 0.035	7.39 ± 0.040	6.49 ± 0.031	5.67 ± 0.025	3.47 ± 0.045	0.02 ± 0.41	Flat
158	19:29:19.76	17:56:43.30	12.00 ± 0.026	10.60 ± 0.028	9.39 ± 0.018	7.53 ± 0.043	7.03 ± 0.048	6.44 ± 0.032	5.02 ± 0.023	2.01 ± 0.044	-0.08 ± 0.10	Flat
159	19:29:30.50	18:01:13.62	15.84 ± 0.067	14.11 ± 0.049	13.13 ± 0.039	11.43 ± 0.048	10.73 ± 0.043	10.18 ± 0.051	9.31 ± 0.023	6.15 ± 0.046	-0.26 ± 0.06	Flat
160	19:29:27.55	18:00:38.05	···	15.60 ± 0.124	13.14 ± 0.040	11.14 ± 0.050	10.42 ± 0.082	9.74 ± 0.055	9.03 ± 0.042	6.45 ± 0.046	-0.41 ± 0.16	II
161	19:29:18.38	17:56:53.41	13.24 ± 0.021	11.68 ± 0.022	10.69 ± 0.021	9.12 ± 0.047	8.44 ± 0.054	7.85 ± 0.038	6.95 ± 0.029	3.88 ± 0.045	-0.31 ± 0.05	II
162	19:29:50.16	18:10:49.62	12.44 ± 0.026	10.04 ± 0.025	8.64 ± 0.018	6.54 ± 0.062	6.38 ± 0.070	5.99 ± 0.031	5.60 ± 0.027	4.10 ± 0.045	-1.31 ± 0.22	II[a]
163	19:29:18.65	17:57:17.53	···	14.70 ± 0.085	12.98 ± 0.038	10.55 ± 0.054	9.49 ± 0.045	8.63 ± 0.039	7.74 ± 0.032	4.09 ± 0.045	0.41 ± 0.17	I
164	19:29:17.52	17:57:17.75	···	15.40 ± 0.092	13.21 ± 0.033	11.92 ± 0.049	11.65 ± 0.091	11.02 ± 0.075	10.97 ± 0.099	6.46 ± 0.048	-0.38 ± 0.22	II
165	19:29:13.09	17:56:32.39	16.91 ± 0.160	15.15 ± 0.079	13.80 ± 0.050	12.38 ± 0.065	11.82 ± 0.084	11.28 ± 0.084	10.45 ± 0.061	6.87 ± 0.046	-0.26 ± 0.06	Flat
166	19:29:21.04	18:00:36.25	13.11 ± 0.020	12.08 ± 0.024	11.44 ± 0.018	10.31 ± 0.038	9.94 ± 0.049	9.64 ± 0.050	9.00 ± 0.044	5.64 ± 0.045	-0.70 ± 0.12	II
167	19:29:04.63	17:54:06.52	···	···	14.41 ± 0.107	13.32 ± 0.071	12.61 ± 0.104	···	···	3.99 ± 0.044	···	I[d]
168	19:29:22.05	18:01:37.09	16.33 ± 0.105	13.63 ± 0.042	12.06 ± 0.029	10.52 ± 0.049	9.85 ± 0.057	9.32 ± 0.047	8.84 ± 0.030	6.08 ± 0.045	-0.67 ± 0.09	II
169	19:29:08.51	17:56:32.89	11.53 ± 0.024	10.74 ± 0.025	10.28 ± 0.020	8.71 ± 0.038	8.20 ± 0.052	7.75 ± 0.035	7.11 ± 0.026	5.25 ± 0.045	-1.03 ± 0.13	II
170	19:29:17.38	18:00:27.11	···	···	···	13.58 ± 0.090	13.13 ± 0.150	···	···	5.96 ± 0.044	···	I[d]
171	19:29:13.07	17:59:24.11	13.78 ± 0.026	12.73 ± 0.027	12.06 ± 0.026	10.98 ± 0.050	10.62 ± 0.056	10.16 ± 0.035	9.20 ± 0.040	5.84 ± 0.044	-0.50 ± 0.10	II
172	19:29:18.60	18:02:08.99	12.09 ± 0.021	9.49 ± 0.022	8.28 ± 0.021	7.48 ± 0.042	7.58 ± 0.051	7.21 ± 0.035	7.10 ± 0.032	6.26 ± 0.044	-2.16 ± 0.08	III
173	19:29:06.17	17:57:19.15	···	14.67 ± 0.096	13.46 ± 0.060	12.31 ± 0.064	11.78 ± 0.116	11.74 ± 0.112	···	4.44 ± 0.044	0.69 ± 0.36	I
174	19:29:00.60	17:55:06.02	···	···	···	12.67 ± 0.194	10.47 ± 0.148	9.20 ± 0.307	···	2.00 ± 0.044	2.01 ± 0.22	I
175	19:28:59.98	17:55:19.27	···	···	···	15.31 ± 0.322	12.99 ± 0.101	12.24 ± 0.240	···	5.64 ± 0.044	1.50 ± 0.25	I
176	19:29:01.06	17:56:07.55	13.06 ± 0.024	11.83 ± 0.021	10.93 ± 0.023	9.78 ± 0.043	9.20 ± 0.032	8.82 ± 0.038	8.00 ± 0.019	4.60 ± 0.044	-0.48 ± 0.08	II
177	19:28:46.13	17:53:27.20	···	···	···	11.90 ± 0.053	10.42 ± 0.060	9.19 ± 0.049	8.42 ± 0.039	4.56 ± 0.045	0.45 ± 0.17	I[a]
178	19:28:45.50	17:53:31.09	···	···	14.58 ± 0.140	···	···	10.25 ± 0.066	9.56 ± 0.035	6.66 ± 0.046	···	No Class
179	19:28:44.66	17:53:21.30	9.26 ± 0.020	6.80 ± 0.020	5.55 ± 0.018	4.85 ± 0.055	···	4.46 ± 0.026	4.42 ± 0.027	4.14 ± 0.045	-2.37 ± 0.14	III[a]
180	19:28:43.26	17:53:36.31	11.06 ± 0.023	10.09 ± 0.021	9.28 ± 0.018	7.79 ± 0.065	7.45 ± 0.037	6.95 ± 0.030	6.08 ± 0.024	3.22 ± 0.044	-0.61 ± 0.05	II[a]
181	19:28:41.46	17:53:10.25	14.24 ± 0.026	13.05 ± 0.023	12.44 ± 0.021	11.56 ± 0.079	11.22 ± 0.061	10.99 ± 0.092	10.14 ± 0.066	6.34 ± 0.045	-0.55 ± 0.18	II
182	19:28:39.24	17:52:58.22	13.17 ± 0.023	11.35 ± 0.021	9.94 ± 0.017	8.30 ± 0.048	7.47 ± 0.044	6.72 ± 0.031	5.90 ± 0.028	3.06 ± 0.044	-0.29 ± 0.10	Flat
183	19:28:38.26	17:52:22.37	···	15.07 ± 0.087	14.20 ± 0.084	12.58 ± 0.063	11.99 ± 0.078	11.33 ± 0.080	10.45 ± 0.063	6.72 ± 0.045	-0.05 ± 0.05	Flat
184	19:28:37.99	17:52:39.47	···	···	12.48 ± 0.025	9.06 ± 0.055	7.65 ± 0.040	6.64 ± 0.032	5.83 ± 0.029	2.45 ± 0.044	0.69 ± 0.38	I
185	19:28:34.54	17:51:35.17	15.51 ± 0.075	13.51 ± 0.044	12.23 ± 0.034	10.38 ± 0.036	9.50 ± 0.051	8.83 ± 0.031	8.06 ± 0.028	6.02 ± 0.045	-0.57 ± 0.20	II
186	19:28:38.47	17:53:27.28	15.12 ± 0.042	13.53 ± 0.030	12.49 ± 0.025	10.85 ± 0.059	10.34 ± 0.056	10.02 ± 0.053	9.13 ± 0.034	5.44 ± 0.044	-0.25 ± 0.10	Flat
187	19:28:36.49	17:54:07.60	···	···	···	13.03 ± 0.075	11.77 ± 0.078	10.96 ± 0.054	10.22 ± 0.047	6.50 ± 0.046	0.12 ± 0.10	Flat
188	19:29:31.52	18:00:34.52	···	···	13.46 ± 0.056	10.74 ± 0.095	9.52 ± 0.083	8.70 ± 0.032	7.97 ± 0.028	2.52 ± 0.044	1.16 ± 0.16	I
189	19:30:00.50	18:00:44.28	13.97 ± 0.025	11.08 ± 0.022	9.70 ± 0.018	8.73 ± 0.040	8.80 ± 0.043	8.47 ± 0.038	8.40 ± 0.031	7.89 ± 0.048	-2.25 ± 0.13	III
190	19:29:11.95	17:45:13.82	15.44 ± 0.046	11.53 ± 0.033	9.66 ± 0.022	8.53 ± 0.043	8.43 ± 0.048	8.04 ± 0.038	8.06 ± 0.028	8.19 ± 0.051	-2.37 ± 0.22	III
191	19:29:22.72	17:50:32.71	15.54 ± 0.067	11.82 ± 0.030	9.91 ± 0.019	8.61 ± 0.041	8.58 ± 0.044	8.14 ± 0.030	8.17 ± 0.032	8.26 ± 0.050	-2.32 ± 0.24	III
192	19:29:29.85	17:53:51.72	···	···	···	13.16 ± 0.082	12.62 ± 0.098	12.15 ± 0.128	11.19 ± 0.078	8.41 ± 0.050	-0.61 ± 0.03	II
193	19:29:42.86	17:59:46.64	9.15 ± 0.021	8.59 ± 0.024	8.41 ± 0.018	8.24 ± 0.050	8.28 ± 0.050	8.24 ± 0.037	8.23 ± 0.029	8.38 ± 0.050	-2.89 ± 0.06	Phot
194	19:29:32.47	17:56:47.69	13.65 ± 0.032	10.66 ± 0.031	9.19 ± 0.021	7.98 ± 0.061	7.97 ± 0.062	7.67 ± 0.034	7.78 ± 0.054	7.25 ± 0.045	-2.24 ± 0.17	III
195	19:29:40.80	18:02:26.52	···	15.53 ± 0.129	13.87 ± 0.056	12.60 ± 0.073	12.45 ± 0.100	11.58 ± 0.122	···	7.19 ± 0.045	-0.30 ± 0.11	II
196	19:29:42.73	18:04:27.88	···	···	12.84 ± 0.024	9.90 ± 0.033	9.07 ± 0.048	8.53 ± 0.027	8.57 ± 0.045	8.23 ± 0.049	-1.36 ± 0.51	II
197	19:29:33.30	18:00:49.61	···	···	···	13.12 ± 0.084	12.22 ± 0.104	11.76 ± 0.103	10.51 ± 0.095	6.57 ± 0.047	0.25 ± 0.06	Flat
198	19:29:11.34	17:51:07.67	13.88 ± 0.030	10.80 ± 0.030	9.31 ± 0.021	8.35 ± 0.064	8.25 ± 0.057	7.98 ± 0.042	7.99 ± 0.034	8.04 ± 0.052	-2.45 ± 0.18	III
199	19:29:20.38	17:55:14.30	···	···	···	14.71 ± 0.144	12.78 ± 0.119	12.26 ± 0.169	12.22 ± 0.339	7.50 ± 0.051	0.28 ± 0.26	Flat
200	19:29:37.73	18:02:51.58	12.91 ± 0.021	10.54 ± 0.022	9.43 ± 0.018	8.61 ± 0.040	8.66 ± 0.051	8.29 ± 0.030	8.22 ± 0.030	7.33 ± 0.045	-2.13 ± 0.08	III
201	19:29:31.95	18:00:41.65	···	15.29 ± 0.093	13.12 ± 0.036	10.19 ± 0.060	8.88 ± 0.076	8.24 ± 0.033	7.62 ± 0.025	3.22 ± 0.045	0.68 ± 0.24	I
202	19:29:32.34	18:00:50.18	···	···	···	13.97 ± 0.090	12.05 ± 0.079	11.05 ± 0.066	10.48 ± 0.062	5.56 ± 0.045	0.90 ± 0.20	I
203	19:29:33.92	18:01:15.24	···	···	13.73 ± 0.045	9.88 ± 0.048	8.93 ± 0.035	8.26 ± 0.036	8.18 ± 0.020	7.77 ± 0.048	-0.94 ± 0.65	II
204	19:29:41.68	18:04:48.83	15.93 ± 0.089	14.27 ± 0.054	13.41 ± 0.045	12.62 ± 0.088	12.08 ± 0.106	11.48 ± 0.156	10.59 ± 0.069	7.26 ± 0.045	-0.48 ± 0.10	II

Table 2—Continued

No	R.A. (J2000)	Decl. (J2000)	J	H	K_s	[3.6]	[4.5]	[5.8]	[8.0]	[24]	α [a]	Class [b]
205	19:29:32.63	18:01:04.12	···	···	···	14.82 ± 0.185	13.81 ± 0.155	···	···	6.64 ± 0.045	···	I[d]
206	19:29:32.35	18:01:12.79	···	···	···	14.81 ± 0.127	12.65 ± 0.088	11.57 ± 0.110	11.02 ± 0.134	6.95 ± 0.046	0.56 ± 0.26	I
207	19:30:00.94	18:14:09.35	14.41 ± 0.030	11.23 ± 0.020	9.69 ± 0.018	8.50 ± 0.045	8.60 ± 0.057	8.28 ± 0.026	8.28 ± 0.032	8.22 ± 0.053	−2.40 ± 0.19	III
208	19:29:30.42	18:00:59.33	14.15 ± 0.026	12.95 ± 0.025	12.38 ± 0.023	11.53 ± 0.043	11.03 ± 0.054	10.60 ± 0.064	9.90 ± 0.049	7.62 ± 0.046	−1.05 ± 0.02	II
209	19:29:30.47	18:02:02.72	14.52 ± 0.031	13.60 ± 0.042	13.22 ± 0.039	12.85 ± 0.049	12.72 ± 0.094	12.34 ± 0.166	···	7.84 ± 0.048	−0.73 ± 0.26	II
210	19:29:11.46	17:53:48.91	16.44 ± 0.116	12.50 ± 0.027	10.63 ± 0.018	9.39 ± 0.033	9.17 ± 0.067	8.72 ± 0.038	8.55 ± 0.027	6.91 ± 0.046	−1.54 ± 0.10	II
211	19:29:23.04	17:59:01.00	···	15.44 ± 0.102	13.83 ± 0.045	11.84 ± 0.062	11.22 ± 0.076	10.70 ± 0.067	9.86 ± 0.056	6.95 ± 0.046	−0.34 ± 0.12	II
212	19:29:58.02	18:15:09.90	16.60 ± 0.135	15.10 ± 0.080	14.58 ± 0.092	14.20 ± 0.112	14.03 ± 0.188	···	···	7.92 ± 0.047	···	No Class
213	19:30:01.40	18:17:17.16	11.58 ± 0.021	9.73 ± 0.022	8.92 ± 0.017	8.53 ± 0.072	8.38 ± 0.053	8.23 ± 0.037	8.24 ± 0.045	8.05 ± 0.048	−2.57 ± 0.08	Phot
214	19:29:50.60	18:13:00.62	12.67 ± 0.022	10.40 ± 0.020	9.36 ± 0.017	8.71 ± 0.029	8.80 ± 0.047	8.45 ± 0.034	8.38 ± 0.032	7.46 ± 0.047	−2.20 ± 0.06	III
215	19:29:06.32	17:54:39.78	···	15.42 ± 0.148	13.66 ± 0.060	11.82 ± 0.048	11.16 ± 0.059	10.72 ± 0.069	9.70 ± 0.040	7.24 ± 0.046	−0.49 ± 0.13	II
216	19:29:22.94	18:02:45.24	13.27 ± 0.038	10.40 ± 0.025	9.09 ± 0.020	8.38 ± 0.081	8.41 ± 0.039	8.05 ± 0.036	8.01 ± 0.024	8.02 ± 0.047	−2.50 ± 0.14	III
217	19:29:25.83	18:04:16.86	11.76 ± 0.021	9.66 ± 0.024	8.80 ± 0.020	8.20 ± 0.035	8.33 ± 0.050	8.02 ± 0.025	7.99 ± 0.029	8.01 ± 0.048	−2.61 ± 0.11	Phot
218	19:29:21.40	18:02:36.92	17.51 ± 0.263	15.16 ± 0.073	14.15 ± 0.059	13.29 ± 0.067	13.24 ± 0.108	12.46 ± 0.199	11.76 ± 0.190	7.04 ± 0.045	−0.13 ± 0.27	Flat
219	19:29:18.55	18:03:17.24	12.89 ± 0.023	10.33 ± 0.022	9.23 ± 0.020	8.53 ± 0.028	8.55 ± 0.045	8.20 ± 0.030	8.21 ± 0.033	7.97 ± 0.046	−2.43 ± 0.12	III
220	19:29:14.73	18:02:02.29	11.58 ± 0.019	9.19 ± 0.022	8.10 ± 0.022	7.46 ± 0.038	7.53 ± 0.045	7.21 ± 0.034	7.16 ± 0.028	6.95 ± 0.046	−2.47 ± 0.11	III
221	19:28:58.22	17:56:54.13	13.08 ± 0.024	10.51 ± 0.018	9.36 ± 0.021	8.55 ± 0.040	8.62 ± 0.045	8.35 ± 0.033	8.30 ± 0.032	7.91 ± 0.048	−2.38 ± 0.11	III
222	19:28:46.87	17:53:15.29	9.18 ± 0.020	8.50 ± 0.026	8.30 ± 0.017	8.23 ± 0.033	8.27 ± 0.052	8.19 ± 0.035	8.09 ± 0.036	8.08 ± 0.048	−2.80 ± 0.04	Phot
223	19:28:42.71	17:53:00.74	···	···	···	14.33 ± 0.134	13.99 ± 0.160	11.40 ± 0.172	10.11 ± 0.151	7.39 ± 0.046	0.49 ± 0.38	I
224	19:28:45.00	17:54:09.00	16.45 ± 0.124	14.81 ± 0.063	13.66 ± 0.043	12.75 ± 0.053	12.14 ± 0.080	11.71 ± 0.074	10.97 ± 0.069	7.26 ± 0.045	−0.42 ± 0.12	II
225	19:28:43.83	17:53:44.70	8.15 ± 0.023	7.32 ± 0.016	7.12 ± 0.016	7.04 ± 0.053	7.16 ± 0.041	7.02 ± 0.033	6.94 ± 0.021	6.96 ± 0.054	−2.82 ± 0.04	Phot
226	19:28:37.73	17:53:13.67	11.97 ± 0.022	9.74 ± 0.023	8.70 ± 0.018	8.10 ± 0.036	8.13 ± 0.044	7.85 ± 0.035	7.82 ± 0.027	7.77 ± 0.046	−2.56 ± 0.11	III
227	19:28:33.89	17:51:57.85	14.24 ± 0.041	13.28 ± 0.037	12.89 ± 0.048	12.42 ± 0.068	12.13 ± 0.089	11.77 ± 0.114	10.64 ± 0.051	7.72 ± 0.047	−0.84 ± 0.16	II
228	19:28:36.55	17:53:27.60	14.00 ± 0.028	13.05 ± 0.032	12.54 ± 0.026	11.54 ± 0.047	11.16 ± 0.067	10.91 ± 0.070	10.40 ± 0.051	7.83 ± 0.047	−1.13 ± 0.06	II
229	19:28:38.57	17:54:27.97	11.74 ± 0.021	10.00 ± 0.019	9.28 ± 0.017	8.80 ± 0.052	8.99 ± 0.049	8.70 ± 0.032	8.62 ± 0.030	8.14 ± 0.048	−2.48 ± 0.06	III
230	19:28:36.19	17:53:47.80	14.21 ± 0.035	13.15 ± 0.040	12.55 ± 0.045	11.61 ± 0.041	11.15 ± 0.062	10.70 ± 0.055	9.86 ± 0.034	8.00 ± 0.050	−1.13 ± 0.06	II
231	19:28:30.98	17:51:49.18	···	···	···	13.49 ± 0.074	12.04 ± 0.056	10.94 ± 0.080	9.98 ± 0.050	6.92 ± 0.045	0.09 ± 0.20	Flat
232	19:29:57.38	17:58:58.33	···	···	14.47 ± 0.087	12.19 ± 0.067	11.14 ± 0.057	10.35 ± 0.076	9.68 ± 0.047	5.85 ± 0.045	0.31 ± 0.15	I
233	19:29:51.87	17:56:50.42	11.72 ± 0.021	10.99 ± 0.023	10.34 ± 0.021	9.10 ± 0.049	8.55 ± 0.050	8.03 ± 0.036	6.84 ± 0.030	4.45 ± 0.044	−0.61 ± 0.08	II
234	19:29:57.84	17:59:30.23	12.85 ± 0.028	11.09 ± 0.026	10.18 ± 0.020	8.96 ± 0.042	8.59 ± 0.039	7.99 ± 0.030	7.20 ± 0.026	4.83 ± 0.044	−0.85 ± 0.04	II
235	19:29:53.52	17:57:50.40	14.06 ± 0.028	12.66 ± 0.027	11.93 ± 0.021	11.13 ± 0.049	10.69 ± 0.059	10.37 ± 0.052	9.66 ± 0.039	5.88 ± 0.045	−0.56 ± 0.17	II
236	19:29:55.04	17:58:41.05	16.36 ± 0.113	14.16 ± 0.051	12.96 ± 0.045	11.76 ± 0.039	11.21 ± 0.062	10.69 ± 0.051	9.63 ± 0.034	5.83 ± 0.045	−0.14 ± 0.10	Flat
237	19:29:52.28	17:57:36.86	···	12.46 ± 0.023	9.80 ± 0.018	8.10 ± 0.049	7.79 ± 0.044	7.31 ± 0.034	7.14 ± 0.023	5.64 ± 0.044	−1.41 ± 0.19	II
238	19:29:51.06	17:57:45.72	···	···	···	13.11 ± 0.061	11.42 ± 0.066	10.78 ± 0.074	10.03 ± 0.056	6.32 ± 0.045	0.15 ± 0.16	Flat
239	19:29:55.02	17:59:35.92	···	14.23 ± 0.045	13.57 ± 0.047	11.90 ± 0.035	11.29 ± 0.063	10.69 ± 0.037	10.12 ± 0.049	6.28 ± 0.045	−0.16 ± 0.09	Flat
240	19:29:49.32	17:58:15.67	14.87 ± 0.035	12.63 ± 0.026	11.09 ± 0.020	8.68 ± 0.037	7.58 ± 0.044	6.60 ± 0.033	5.64 ± 0.024	2.36 ± 0.044	0.35 ± 0.20	I
241	19:29:16.47	17:44:01.50	···	···	14.47 ± 0.101	12.35 ± 0.054	11.47 ± 0.071	10.59 ± 0.062	9.78 ± 0.052	6.51 ± 0.045	0.09 ± 0.14	Flat
242	19:29:49.69	17:58:59.48	12.89 ± 0.025	11.60 ± 0.027	10.94 ± 0.022	9.94 ± 0.041	9.61 ± 0.046	9.39 ± 0.041	8.93 ± 0.056	6.08 ± 0.045	−1.08 ± 0.10	II
243	19:29:31.18	17:51:02.23	13.48 ± 0.032	10.47 ± 0.030	9.04 ± 0.023	8.10 ± 0.051	7.93 ± 0.056	7.58 ± 0.035	7.39 ± 0.035	5.92 ± 0.045	−1.75 ± 0.07	III
244	19:29:48.90	17:58:55.09	···	···	14.65 ± 0.109	12.78 ± 0.083	11.27 ± 0.072	10.06 ± 0.047	9.15 ± 0.039	4.39 ± 0.044	1.05 ± 0.11	I
245	19:29:44.02	17:58:46.60	···	···	···	13.46 ± 0.105	11.85 ± 0.108	12.16 ± 0.226	···	6.81 ± 0.045	0.17 ± 0.23	Flat
246	19:29:46.68	18:00:28.40	···	14.79 ± 0.060	13.22 ± 0.031	11.77 ± 0.050	10.87 ± 0.063	10.17 ± 0.050	9.31 ± 0.060	5.27 ± 0.045	0.16 ± 0.05	Flat
247	19:29:44.98	17:59:57.30	9.23 ± 0.020	7.27 ± 0.029	6.42 ± 0.017	5.87 ± 0.046	6.35 ± 0.077	5.77 ± 0.028	5.78 ± 0.028	5.67 ± 0.045	−2.61 ± 0.11	Phot[a]
248	19:29:45.80	18:00:55.08	13.44 ± 0.026	11.51 ± 0.026	10.07 ± 0.020	8.73 ± 0.038	8.23 ± 0.047	7.71 ± 0.039	6.97 ± 0.027	2.77 ± 0.044	−0.11 ± 0.13	Flat
249	19:29:39.71	17:58:36.95	···	···	···	15.30 ± 0.176	13.28 ± 0.123	···	···	6.75 ± 0.045	···	I[d]
250	19:29:17.93	17:50:09.53	···	15.07 ± 0.068	13.56 ± 0.033	12.62 ± 0.053	12.33 ± 0.075	11.97 ± 0.109	11.58 ± 0.135	4.95 ± 0.044	0.43 ± 0.46	I
251	19:30:00.97	18:08:50.78	15.92 ± 0.084	···	···	10.13 ± 0.038	10.01 ± 0.053	9.53 ± 0.040	8.91 ± 0.064	6.37 ± 0.045	−1.07 ± 0.07	II
252	19:29:38.04	17:59:25.98	15.76 ± 0.071	13.95 ± 0.052	12.96 ± 0.037	11.78 ± 0.040	11.35 ± 0.062	10.96 ± 0.055	9.98 ± 0.038	5.76 ± 0.045	−0.13 ± 0.17	Flat
253	19:29:23.13	17:53:03.01	13.65 ± 0.058	12.39 ± 0.039	11.64 ± 0.032	10.40 ± 0.116	9.91 ± 0.066	9.68 ± 0.051	9.12 ± 0.021	6.56 ± 0.045	−1.01 ± 0.07	II
254	19:29:24.81	17:53:53.56	11.74 ± 0.026	9.03 ± 0.027	7.74 ± 0.029	6.92 ± 0.053	6.96 ± 0.044	6.57 ± 0.029	6.49 ± 0.020	5.94 ± 0.045	−2.23 ± 0.11	III[a]
255	19:29:49.74	18:04:55.42	14.59 ± 0.036	12.55 ± 0.027	11.03 ± 0.020	9.08 ± 0.040	8.31 ± 0.041	7.74 ± 0.033	7.05 ± 0.026	3.09 ± 0.044	0.06 ± 0.10	Flat

Table 2—Continued

No	R.A. (J2000)	Decl. (J2000)	J	H	K_s	[3.6]	[4.5]	[5.8]	[8.0]	[24]	α [a]	Class [b]
256	19:29:47.24	18:04:13.22	···	···	···	14.76 ± 0.095	13.25 ± 0.183	12.61 ± 0.262	···	5.89 ± 0.045	1.30 ± 0.10	I
257	19:29:40.91	18:01:28.24	···	···	14.43 ± 0.072	12.03 ± 0.051	10.85 ± 0.057	10.31 ± 0.048	9.43 ± 0.028	6.09 ± 0.045	0.18 ± 0.20	Flat
258	19:29:26.39	17:55:22.26	···	14.34 ± 0.050	12.40 ± 0.028	9.89 ± 0.050	9.14 ± 0.053	8.23 ± 0.040	7.37 ± 0.031	4.52 ± 0.044	0.01 ± 0.22	Flat
259	19:29:39.58	18:01:29.21	14.33 ± 0.036	12.34 ± 0.027	10.91 ± 0.020	8.78 ± 0.049	8.13 ± 0.047	7.46 ± 0.031	6.52 ± 0.027	2.47 ± 0.044	0.26 ± 0.08	Flat
260	19:29:33.43	17:58:49.26	16.24 ± 0.099	13.41 ± 0.070	11.78 ± 0.037	9.87 ± 0.036	9.26 ± 0.052	8.69 ± 0.041	7.98 ± 0.023	5.47 ± 0.044	−0.56 ± 0.14	II
261	19:29:34.11	17:59:21.52	···	···	···	12.73 ± 0.064	9.95 ± 0.049	8.21 ± 0.038	7.18 ± 0.027	2.92 ± 0.044	1.36 ± 0.42	I
262	19:29:50.08	18:06:18.07	···	12.12 ± 0.020	9.44 ± 0.018	7.62 ± 0.051	7.44 ± 0.035	6.87 ± 0.031	6.77 ± 0.020	5.40 ± 0.045	−1.47 ± 0.21	II
263	19:29:14.22	17:50:55.68	···	···	···	13.99 ± 0.094	12.01 ± 0.073	10.75 ± 0.082	10.08 ± 0.109	4.62 ± 0.045	1.37 ± 0.20	I
264	19:29:47.12	18:05:28.61	···	···	13.78 ± 0.070	10.92 ± 0.070	9.08 ± 0.062	8.17 ± 0.033	7.33 ± 0.030	2.43 ± 0.044	1.30 ± 0.24	I
265	19:29:49.81	18:06:35.96	15.08 ± 0.049	13.46 ± 0.035	12.60 ± 0.026	11.97 ± 0.059	11.39 ± 0.087	10.81 ± 0.080	9.78 ± 0.048	5.62 ± 0.044	−0.12 ± 0.19	Flat
266	19:29:22.09	17:54:44.06	11.37 ± 0.029	10.43 ± 0.028	9.52 ± 0.021	8.20 ± 0.036	7.67 ± 0.044	7.12 ± 0.033	5.94 ± 0.020	3.25 ± 0.044	−0.47 ± 0.06	II
267	19:29:50.52	18:07:26.26	···	···	···	14.52 ± 0.191	12.61 ± 0.092	11.73 ± 0.121	11.10 ± 0.164	5.59 ± 0.045	1.19 ± 0.19	I
268	19:29:34.08	18:00:15.37	14.69 ± 0.047	13.11 ± 0.038	12.26 ± 0.028	10.90 ± 0.035	10.43 ± 0.048	9.81 ± 0.046	9.20 ± 0.031	5.83 ± 0.044	−0.46 ± 0.06	II
269	19:29:32.72	17:59:44.23	···	···	13.93 ± 0.058	11.80 ± 0.060	10.80 ± 0.060	10.20 ± 0.060	9.05 ± 0.055	4.07 ± 0.044	0.84 ± 0.09	I[a]
270	19:29:32.24	17:59:49.88	16.86 ± 0.166	14.23 ± 0.070	12.66 ± 0.046	9.95 ± 0.068	9.23 ± 0.067	8.67 ± 0.043	7.69 ± 0.039	3.97 ± 0.045	0.27 ± 0.18	Flat[a]
271	19:29:25.51	17:56:44.59	12.25 ± 0.027	11.90 ± 0.027	11.75 ± 0.021	11.34 ± 0.058	11.12 ± 0.075	10.22 ± 0.138	···	5.86 ± 0.044	−0.50 ± 0.22	II
272	19:29:37.05	18:01:47.42	···	···	···	14.33 ± 0.110	12.50 ± 0.089	11.59 ± 0.122	10.23 ± 0.061	5.77 ± 0.044	1.04 ± 0.16	I
273	19:29:34.03	18:00:29.95	16.70 ± 0.139	14.72 ± 0.057	13.65 ± 0.043	12.60 ± 0.066	11.88 ± 0.074	11.25 ± 0.080	10.07 ± 0.043	6.41 ± 0.045	−0.06 ± 0.08	Flat
274	19:29:34.48	18:00:52.63	14.42 ± 0.028	12.56 ± 0.029	11.47 ± 0.028	10.15 ± 0.038	9.58 ± 0.055	9.23 ± 0.029	8.56 ± 0.026	5.38 ± 0.045	−0.60 ± 0.06	II
275	19:29:34.01	18:00:40.18	16.52 ± 0.116	13.53 ± 0.042	11.65 ± 0.027	9.47 ± 0.057	8.54 ± 0.043	8.01 ± 0.034	7.47 ± 0.023	5.56 ± 0.045	−0.68 ± 0.27	II
276	19:30:04.60	18:02:33.14	11.98 ± 0.045	9.91 ± 0.032	8.94 ± 0.028	8.28 ± 0.039	8.43 ± 0.039	8.13 ± 0.030	8.15 ± 0.022	8.07 ± 0.047	−2.59 ± 0.11	Phot
277	19:29:51.93	17:57:13.54	···	···	···	13.39 ± 0.066	12.51 ± 0.097	11.65 ± 0.110	10.75 ± 0.066	7.41 ± 0.046	−0.07 ± 0.05	Flat
278	19:29:48.58	17:58:00.91	14.98 ± 0.041	13.74 ± 0.032	12.85 ± 0.033	11.83 ± 0.053	11.52 ± 0.063	10.91 ± 0.071	10.07 ± 0.047	7.97 ± 0.048	−1.00 ± 0.05	II
279	19:29:48.01	17:58:17.26	15.69 ± 0.066	14.50 ± 0.050	14.12 ± 0.066	13.09 ± 0.063	12.84 ± 0.119	12.05 ± 0.136	11.08 ± 0.116	8.02 ± 0.048	−0.51 ± 0.08	II
280	19:29:52.15	18:00:52.81	12.31 ± 0.020	9.71 ± 0.022	8.56 ± 0.018	7.89 ± 0.064	7.94 ± 0.046	7.61 ± 0.037	7.59 ± 0.030	7.63 ± 0.046	−2.55 ± 0.13	III
281	19:29:33.74	17:52:53.51	9.61 ± 0.026	8.94 ± 0.051	8.66 ± 0.018	8.52 ± 0.044	8.73 ± 0.053	8.60 ± 0.038	8.42 ± 0.030	7.80 ± 0.047	−2.57 ± 0.05	Phot
282	19:29:43.72	17:57:43.09	10.16 ± 0.020	8.28 ± 0.018	7.46 ± 0.021	6.92 ± 0.041	7.07 ± 0.042	6.84 ± 0.037	6.78 ± 0.024	6.92 ± 0.045	−2.70 ± 0.11	Phot[a]
283	19:29:25.71	17:50:21.12	15.89 ± 0.083	14.73 ± 0.075	14.04 ± 0.094	13.19 ± 0.059	12.72 ± 0.118	12.30 ± 0.144	11.41 ± 0.105	8.09 ± 0.047	−0.59 ± 0.11	II
284	19:29:22.85	17:49:17.47	13.26 ± 0.024	10.27 ± 0.027	8.94 ± 0.019	8.09 ± 0.040	8.16 ± 0.044	7.82 ± 0.037	7.82 ± 0.029	7.88 ± 0.048	−2.52 ± 0.16	III
285	19:29:27.92	17:51:39.96	12.02 ± 0.026	9.49 ± 0.027	8.38 ± 0.031	7.60 ± 0.047	7.74 ± 0.035	7.41 ± 0.031	7.39 ± 0.018	7.32 ± 0.046	−2.51 ± 0.13	III
286	19:29:30.23	17:52:40.73	12.85 ± 0.026	10.18 ± 0.028	9.01 ± 0.019	8.29 ± 0.055	8.34 ± 0.044	8.01 ± 0.033	8.02 ± 0.031	7.97 ± 0.049	−2.52 ± 0.13	III
287	19:29:52.93	18:02:49.13	13.77 ± 0.028	13.01 ± 0.028	12.73 ± 0.028	12.21 ± 0.055	12.05 ± 0.107	11.94 ± 0.114	10.98 ± 0.070	7.17 ± 0.045	−0.73 ± 0.26	II
288	19:29:20.13	17:49:09.34	12.22 ± 0.026	9.68 ± 0.027	8.59 ± 0.019	7.86 ± 0.054	7.93 ± 0.046	7.65 ± 0.035	7.63 ± 0.026	7.70 ± 0.046	−2.58 ± 0.14	Phot
289	19:29:19.78	17:49:56.17	14.11 ± 0.029	10.70 ± 0.028	9.10 ± 0.019	8.13 ± 0.031	8.14 ± 0.050	7.74 ± 0.034	7.70 ± 0.028	7.73 ± 0.048	−2.40 ± 0.18	III
290	19:29:38.76	17:58:58.33	···	···	···	13.16 ± 0.057	12.49 ± 0.081	12.20 ± 0.171	···	7.91 ± 0.048	−0.37 ± 0.08	II
291	19:29:50.23	18:04:15.92	15.61 ± 0.056	14.42 ± 0.044	13.77 ± 0.051	12.74 ± 0.054	12.16 ± 0.078	11.56 ± 0.069	10.95 ± 0.100	8.05 ± 0.049	−0.70 ± 0.03	II
292	19:29:37.20	17:59:11.62	15.65 ± 0.051	13.94 ± 0.040	12.93 ± 0.033	11.46 ± 0.073	11.07 ± 0.063	10.70 ± 0.066	10.09 ± 0.058	7.08 ± 0.046	−0.72 ± 0.08	II
293	19:29:37.89	18:00:03.53	14.78 ± 0.037	···	···	11.61 ± 0.060	11.21 ± 0.061	10.93 ± 0.067	10.03 ± 0.052	7.11 ± 0.045	−0.77 ± 0.07	II
294	19:29:46.52	18:03:57.49	13.62 ± 0.021	10.35 ± 0.023	8.80 ± 0.018	7.85 ± 0.051	7.91 ± 0.042	7.48 ± 0.039	7.47 ± 0.031	7.20 ± 0.045	−2.32 ± 0.15	III
295	19:29:50.89	18:06:07.92	14.26 ± 0.038	12.92 ± 0.041	···	11.76 ± 0.044	11.58 ± 0.085	11.37 ± 0.091	11.38 ± 0.107	7.26 ± 0.045	−1.22 ± 0.32	II
296	19:29:54.24	18:07:42.49	10.90 ± 0.022	9.04 ± 0.023	8.24 ± 0.027	7.79 ± 0.050	7.94 ± 0.045	7.64 ± 0.035	7.61 ± 0.026	7.57 ± 0.046	−2.64 ± 0.09	Phot
297	19:29:44.61	18:03:48.38	···	10.83 ± 0.027	9.01 ± 0.074	9.14 ± 0.039	9.27 ± 0.055	8.94 ± 0.038	8.94 ± 0.033	8.18 ± 0.047	−2.56 ± 0.07	Phot
298	19:29:20.04	17:53:31.67	13.39 ± 0.026	10.47 ± 0.027	9.10 ± 0.019	8.32 ± 0.040	8.40 ± 0.046	8.02 ± 0.039	8.02 ± 0.030	8.17 ± 0.050	−2.55 ± 0.16	III
299	19:29:51.95	18:07:39.07	14.49 ± 0.026	11.18 ± 0.020	9.44 ± 0.017	8.49 ± 0.052	8.50 ± 0.044	8.09 ± 0.032	8.05 ± 0.033	8.06 ± 0.047	−2.40 ± 0.18	III
300	19:29:59.06	18:10:50.99	14.45 ± 0.035	13.54 ± 0.031	13.06 ± 0.037	12.55 ± 0.051	12.27 ± 0.077	···	11.25 ± 0.096	7.90 ± 0.048	−0.89 ± 0.18	II
301	19:30:00.57	18:11:46.14	10.23 ± 0.022	8.72 ± 0.027	8.11 ± 0.018	7.71 ± 0.039	7.85 ± 0.053	7.62 ± 0.030	7.62 ± 0.033	7.38 ± 0.047	−2.63 ± 0.06	Phot
302	19:29:41.30	18:03:29.59	···	···	14.24 ± 0.067	12.90 ± 0.071	12.25 ± 0.102	11.69 ± 0.105	10.89 ± 0.067	7.69 ± 0.047	−0.39 ± 0.02	II
303	19:29:34.82	18:00:42.66	···	···	···	13.35 ± 0.088	12.43 ± 0.179	11.79 ± 0.205	11.23 ± 0.098	7.85 ± 0.049	−0.34 ± 0.07	II
304	19:29:19.10	17:53:58.56	···	···	14.01 ± 0.061	12.80 ± 0.066	12.48 ± 0.099	12.05 ± 0.121	11.34 ± 0.092	7.81 ± 0.047	−0.55 ± 0.11	II
305	19:29:16.85	17:53:15.86	16.49 ± 0.151	15.19 ± 0.095	14.59 ± 0.098	14.03 ± 0.149	13.87 ± 0.158	···	11.56 ± 0.111	7.99 ± 0.050	−0.22 ± 0.23	Flat
306	19:30:21.98	17:37:32.34	···	13.95 ± 0.057	10.52 ± 0.024	8.36 ± 0.030	7.91 ± 0.050	7.38 ± 0.027	7.31 ± 0.026	5.89 ± 0.045	−1.28 ± 0.28	II

Table 2—Continued

No	R.A. (J2000)	Decl. (J2000)	J	H	K_s	[3.6]	[4.5]	[5.8]	[8.0]	[24]	α [a]	Class [b]
307	19:30:18.06	17:38:04.78	···	···	···	12.05 ± 0.050	10.72 ± 0.061	9.88 ± 0.048	9.32 ± 0.068	5.48 ± 0.045	0.11 ± 0.12	Flat
308	19:30:18.32	17:38:13.13	···	···	···	14.87 ± 0.130	13.61 ± 0.139	12.76 ± 0.251	···	6.79 ± 0.045	0.93 ± 0.06	I
309	19:30:16.60	17:38:43.04	···	···	···	13.88 ± 0.111	13.48 ± 0.139	···	···	6.12 ± 0.045	···	I[d]
310	19:30:14.21	17:38:06.32	16.08 ± 0.105	11.56 ± 0.029	9.27 ± 0.021	7.93 ± 0.037	7.78 ± 0.049	7.30 ± 0.035	7.29 ± 0.027	6.98 ± 0.045	−2.08 ± 0.22	III
311	19:30:13.92	17:39:03.60	13.73 ± 0.030	11.96 ± 0.033	10.59 ± 0.023	8.46 ± 0.036	7.43 ± 0.042	6.55 ± 0.035	5.56 ± 0.027	2.54 ± 0.044	0.13 ± 0.18	Flat
312	19:30:13.86	17:39:34.99	12.37 ± 0.021	9.38 ± 0.028	8.03 ± 0.029	7.19 ± 0.042	7.21 ± 0.043	6.85 ± 0.038	6.83 ± 0.030	6.72 ± 0.045	−2.41 ± 0.15	III
313	19:30:14.10	17:40:45.77	13.59 ± 0.024	10.41 ± 0.032	8.88 ± 0.020	7.87 ± 0.050	7.84 ± 0.048	7.40 ± 0.033	7.26 ± 0.024	5.67 ± 0.044	−1.72 ± 0.07	III
314	19:30:10.14	17:39:03.13	···	12.96 ± 0.035	10.06 ± 0.022	8.29 ± 0.035	7.96 ± 0.046	7.38 ± 0.030	7.23 ± 0.024	5.69 ± 0.045	−1.33 ± 0.20	II
315	19:30:05.42	17:38:05.60	11.14 ± 0.023	8.57 ± 0.033	7.40 ± 0.024	6.72 ± 0.039	6.73 ± 0.049	6.36 ± 0.032	6.34 ± 0.028	6.05 ± 0.045	−2.39 ± 0.11	III[a]
316	19:30:08.91	17:41:03.44	11.81 ± 0.023	8.61 ± 0.024	7.01 ± 0.024	6.08 ± 0.042	6.05 ± 0.046	5.59 ± 0.029	5.45 ± 0.028	3.78 ± 0.044	−1.70 ± 0.06	III[a]
317	19:30:02.50	17:38:52.55	12.30 ± 0.025	9.80 ± 0.026	8.70 ± 0.022	8.02 ± 0.049	8.00 ± 0.049	7.68 ± 0.034	7.60 ± 0.027	6.84 ± 0.045	−2.21 ± 0.07	III
318	19:30:07.59	17:53:53.92	···	···	14.21 ± 0.097	12.23 ± 0.066	11.57 ± 0.087	10.81 ± 0.067	9.67 ± 0.038	5.81 ± 0.045	0.29 ± 0.05	Flat
319	19:30:07.65	17:54:07.16	14.70 ± 0.045	12.75 ± 0.031	11.39 ± 0.020	9.62 ± 0.041	8.74 ± 0.045	7.97 ± 0.037	7.19 ± 0.027	4.38 ± 0.044	−0.25 ± 0.13	Flat
320	19:30:05.75	17:53:48.55	8.92 ± 0.039	6.56 ± 0.040	5.49 ± 0.020	4.89 ± 0.067	···	4.53 ± 0.028	4.30 ± 0.019	3.13 ± 0.044	−2.02 ± 0.04	III[a]
321	19:30:10.43	17:56:47.40	···	···	···	14.24 ± 0.142	13.02 ± 0.117	12.13 ± 0.157	11.35 ± 0.067	6.57 ± 0.045	0.71 ± 0.09	I
322	19:30:08.22	17:56:35.34	9.35 ± 0.023	6.80 ± 0.026	5.60 ± 0.017	4.80 ± 0.058	···	4.40 ± 0.031	4.00 ± 0.028	2.44 ± 0.044	−1.71 ± 0.04	III[a]
323	19:30:02.15	17:55:00.73	11.76 ± 0.034	9.81 ± 0.035	8.60 ± 0.026	6.90 ± 0.145	6.46 ± 0.047	5.84 ± 0.038	4.91 ± 0.026	1.57 ± 0.044	−0.24 ± 0.05	Flat[a]
324	19:30:12.67	17:59:31.92	12.09 ± 0.022	9.21 ± 0.019	7.84 ± 0.022	6.89 ± 0.051	6.95 ± 0.046	6.50 ± 0.028	6.20 ± 0.024	3.88 ± 0.044	−1.43 ± 0.09	II[a]
325	19:30:00.54	17:54:35.17	13.84 ± 0.026	10.59 ± 0.031	8.82 ± 0.022	7.36 ± 0.034	7.21 ± 0.045	6.72 ± 0.033	6.58 ± 0.029	5.69 ± 0.044	−1.77 ± 0.19	III
326	19:30:06.38	17:57:30.92	···	14.42 ± 0.084	12.65 ± 0.042	10.11 ± 0.055	9.06 ± 0.075	8.67 ± 0.036	8.17 ± 0.040	4.74 ± 0.045	−0.06 ± 0.23	Flat
327	19:30:05.22	17:57:27.29	···	···	14.88 ± 0.122	12.13 ± 0.057	9.86 ± 0.046	8.74 ± 0.034	7.86 ± 0.035	3.16 ± 0.044	1.48 ± 0.30	I
328	19:30:00.20	17:56:02.00	13.61 ± 0.029	11.59 ± 0.032	9.86 ± 0.023	7.04 ± 0.033	6.28 ± 0.067	5.41 ± 0.028	4.42 ± 0.023	0.92 ± 0.044	0.37 ± 0.21	I[a]
329	19:30:02.76	17:57:19.19	···	···	···	···	13.99 ± 0.308	11.78 ± 0.128	10.44 ± 0.164	6.11 ± 0.045	1.16 ± 0.27	I
330	19:29:59.24	17:58:25.18	···	15.05 ± 0.074	13.29 ± 0.037	11.31 ± 0.044	10.35 ± 0.048	9.69 ± 0.051	8.83 ± 0.040	5.05 ± 0.045	0.20 ± 0.09	Flat
331	19:29:50.53	17:55:13.80	13.19 ± 0.036	10.50 ± 0.027	9.20 ± 0.018	8.29 ± 0.045	8.20 ± 0.045	7.89 ± 0.036	7.76 ± 0.027	6.94 ± 0.045	−2.07 ± 0.10	III
332	19:30:20.75	17:39:20.20	13.84 ± 0.056	12.67 ± 0.043	12.06 ± 0.036	11.67 ± 0.049	11.60 ± 0.074	11.22 ± 0.082	10.13 ± 0.074	7.10 ± 0.045	−0.92 ± 0.20	II
333	19:30:17.77	17:38:29.11	15.73 ± 0.088	14.16 ± 0.058	13.11 ± 0.044	11.80 ± 0.059	11.25 ± 0.096	10.79 ± 0.080	9.97 ± 0.047	6.89 ± 0.045	−0.53 ± 0.04	II
334	19:30:14.07	17:38:51.83	14.66 ± 0.035	13.83 ± 0.045	13.39 ± 0.046	12.48 ± 0.067	12.00 ± 0.078	11.49 ± 0.097	10.68 ± 0.099	6.68 ± 0.055	−0.29 ± 0.16	Flat
335	19:30:19.78	17:41:27.49	10.53 ± 0.019	8.97 ± 0.029	8.35 ± 0.021	7.99 ± 0.043	8.13 ± 0.047	7.92 ± 0.035	7.87 ± 0.029	7.95 ± 0.049	−2.74 ± 0.08	Phot
336	19:30:17.96	17:43:46.24	11.15 ± 0.021	9.18 ± 0.028	8.33 ± 0.029	7.82 ± 0.046	7.91 ± 0.051	7.71 ± 0.035	7.69 ± 0.030	7.75 ± 0.047	−2.68 ± 0.10	Phot
337	19:30:06.99	17:40:13.08	···	15.28 ± 0.131	13.89 ± 0.069	12.39 ± 0.054	11.91 ± 0.091	11.56 ± 0.091	11.01 ± 0.073	7.00 ± 0.045	−0.33 ± 0.14	II
338	19:30:15.57	17:44:39.37	14.38 ± 0.037	12.88 ± 0.040	11.93 ± 0.024	11.26 ± 0.051	10.84 ± 0.062	10.54 ± 0.064	10.02 ± 0.051	7.02 ± 0.044	−1.01 ± 0.11	II
339	19:30:10.98	17:42:24.37	13.46 ± 0.040	12.25 ± 0.049	11.66 ± 0.043	10.74 ± 0.055	10.10 ± 0.114	10.05 ± 0.046	9.65 ± 0.036	7.14 ± 0.045	−1.21 ± 0.08	II
340	19:30:04.17	17:40:01.20	10.20 ± 0.023	8.89 ± 0.026	8.43 ± 0.020	8.14 ± 0.053	8.25 ± 0.046	8.10 ± 0.033	8.04 ± 0.027	8.15 ± 0.047	−2.79 ± 0.07	Phot
341	19:30:14.25	17:45:09.94	···	14.65 ± 0.068	13.05 ± 0.029	11.88 ± 0.039	11.21 ± 0.065	10.93 ± 0.048	10.61 ± 0.052	6.81 ± 0.044	−0.56 ± 0.15	II
342	19:30:08.40	17:54:27.54	13.88 ± 0.034	12.28 ± 0.036	11.57 ± 0.026	10.92 ± 0.055	10.56 ± 0.050	10.33 ± 0.063	9.91 ± 0.040	8.23 ± 0.049	−1.62 ± 0.02	III
343	19:30:06.17	17:57:09.11	13.77 ± 0.031	12.57 ± 0.028	11.94 ± 0.023	10.98 ± 0.037	10.59 ± 0.064	10.29 ± 0.051	9.74 ± 0.045	7.16 ± 0.045	−1.09 ± 0.06	II
344	19:30:09.34	17:58:40.51	12.93 ± 0.037	10.26 ± 0.033	9.09 ± 0.028	8.34 ± 0.032	8.29 ± 0.047	8.00 ± 0.031	7.95 ± 0.026	7.68 ± 0.046	−2.38 ± 0.12	III
345	19:30:03.27	17:56:25.87	···	···	···	14.58 ± 0.126	14.10 ± 0.192	···	···	7.07 ± 0.045	···	No Class
346	19:29:54.72	17:53:44.77	14.63 ± 0.049	13.56 ± 0.059	12.93 ± 0.053	12.65 ± 0.068	12.41 ± 0.097	···	···	7.99 ± 0.047	···	No Class
347	19:30:12.59	18:01:59.77	11.35 ± 0.021	9.38 ± 0.019	8.56 ± 0.018	8.09 ± 0.035	8.16 ± 0.047	7.90 ± 0.036	7.91 ± 0.027	8.02 ± 0.047	−2.69 ± 0.11	Phot
348	19:30:03.68	17:59:08.27	14.44 ± 0.037	13.52 ± 0.048	12.99 ± 0.050	12.25 ± 0.062	11.91 ± 0.082	11.23 ± 0.095	10.30 ± 0.056	7.92 ± 0.047	−0.89 ± 0.07	II
349	19:29:54.72	17:55:41.81	10.98 ± 0.023	9.08 ± 0.028	8.34 ± 0.022	7.89 ± 0.046	8.03 ± 0.072	7.78 ± 0.037	7.74 ± 0.031	7.80 ± 0.047	−2.69 ± 0.09	Phot
350	19:29:58.18	17:57:22.54	13.78 ± 0.036	12.58 ± 0.047	11.66 ± 0.028	10.82 ± 0.057	10.22 ± 0.095	10.01 ± 0.074	9.50 ± 0.041	7.43 ± 0.045	−1.29 ± 0.04	II
351	19:29:59.29	17:56:24.29	···	···	···	12.19 ± 0.068	10.61 ± 0.063	9.90 ± 0.057	9.08 ± 0.049	3.12 ± 0.044	1.36 ± 0.17	I
352	19:30:15.55	17:38:45.74	···	···	···	15.74 ± 0.227	13.47 ± 0.113	12.38 ± 0.178	12.02 ± 0.244	5.75 ± 0.044	1.62 ± 0.27	I
353	19:29:59.14	17:56:18.53	12.15 ± 0.034	10.90 ± 0.038	10.19 ± 0.033	8.68 ± 0.088	8.17 ± 0.089	7.74 ± 0.050	6.97 ± 0.035	3.09 ± 0.044	−0.22 ± 0.10	Flat
354	19:30:15.93	17:38:44.77	···	···	···	12.82 ± 0.066	11.32 ± 0.126	10.54 ± 0.098	9.49 ± 0.076	5.37 ± 0.045	0.54 ± 0.11	I
355	19:30:10.14	18:19:53.04	···	···	···	15.59 ± 0.322	13.09 ± 0.129	···	···	5.06 ± 0.046	···	I[a,d]
356	19:30:07.76	18:20:10.61	···	···	···	14.63 ± 0.179	14.56 ± 0.327	···	···	6.52 ± 0.044	···	I[a,d]
357	19:30:43.69	18:26:15.86	···	···	···	13.54 ± 0.159	12.21 ± 0.127	11.60 ± 0.113	11.59 ± 0.161	4.50 ± 0.044	1.38 ± 0.37	I[a]

Table 2—Continued

No	R.A. (J2000)	Decl. (J2000)	J	H	K_s	[3.6]	[4.5]	[5.8]	[8.0]	[24]	α [a]	Class [b]
358	19:30:18.90	18:17:47.90	11.73 ± 0.022	11.14 ± 0.023	10.79 ± 0.022	10.37 ± 0.171	9.95 ± 0.170	9.31 ± 0.339	···	1.62 ± 0.044	0.92 ± 0.46	I[a]
359	19:29:20.25	17:55:01.02	···	···	···	11.63 ± 0.109	9.94 ± 0.089	8.72 ± 0.039	7.31 ± 0.039	3.12 ± 0.044	1.03 ± 0.19	I[a]
360	19:29:34.15	18:01:39.83	···	···	···	15.12 ± 0.210	12.69 ± 0.157	12.32 ± 0.242	···	4.14 ± 0.044	2.19 ± 0.24	I[a]
361	19:29:20.64	17:57:18.90	···	14.71 ± 0.153	12.56 ± 0.056	10.57 ± 0.143	8.63 ± 0.124	8.19 ± 0.049	7.43 ± 0.031	3.39 ± 0.044	0.53 ± 0.21	I[a]
362	19:28:41.48	17:53:28.75	···	···	···	15.04 ± 0.176	14.12 ± 0.272	···	···	6.26 ± 0.044	···	I[a,d]
363	19:29:17.99	17:43:54.80	···	···	···	···	13.53 ± 0.153	···	···	6.18 ± 0.045	···	I[a,d]
364	19:29:37.46	17:58:01.09	7.79 ± 0.029	5.49 ± 0.022	4.43 ± 0.022	3.95 ± 0.071	4.06 ± 0.064	3.59 ± 0.034	3.45 ± 0.043	2.55 ± 0.044	-2.18 ± 0.05	III[a]
365	19:29:49.63	18:04:41.95	···	···	···	···	13.89 ± 0.143	···	···	5.36 ± 0.044	···	I[a,d]
366	19:29:26.03	17:54:52.16	···	···	···	···	9.90 ± 0.175	···	···	1.68 ± 0.044	···	I[a,d]
367	19:29:35.06	17:59:08.34	···	···	···	···	13.00 ± 0.188	···	···	6.27 ± 0.045	···	I[a,d]
368	19:29:59.01	17:58:40.08	···	···	···	···	14.37 ± 0.188	···	11.81 ± 0.120	5.66 ± 0.044	···	I[a,d]
369	19:30:05.49	17:57:23.54	···	···	···	15.56 ± 0.316	13.89 ± 0.214	12.49 ± 0.251	···	4.56 ± 0.047	2.32 ± 0.08	I[a]

[a] Defined as $\alpha = d \log(\lambda F_\lambda)/d \log(\lambda)$ (Lada 1987) between 2 and 24 μm.

[b] a = IRAC magnitudes are from the GLIMPSEI Archive; d = a deeply embedded protostar

Table 3. Saturated Sources in 24 μm

No	R.A. (J2000)	Decl. (J2000)	J	H	K_s	[3.6]	[4.5]	[5.8]	[8.0]/*MSX* A	*MSX* E	α	Class
1	19:29:17.59	17:56:22.81	···	···	11.92 ± 0.073	7.03 ± 0.106	4.42 ± 0.110	3.54 ± 0.050	2.36 ± 0.045	-1.39 ± 0.065	1.88 ± 0.62	I
2	19:29:17.29	17:56:17.59	···	14.85 ± 0.181	11.97 ± 0.091	8.88 ± 0.204	7.49 ± 0.162	6.19 ± 0.046	4.97 ± 0.044	...	2.21 ± 0.13	I
3	19:29:41.28	18:06:39.38	8.19 ± 0.027	5.83 ± 0.023	4.63 ± 0.020	···	2.85 ± 0.165	2.55 ± 0.035	1.78 ± 0.045	0.17 ± 0.066	-1.11 ± 0.09	II
4	19:30:01.68	18:19:14.23	8.73 ± 0.032	6.23 ± 0.020	4.81 ± 0.021	4.45 ± 0.160	···	···	1.46 ± 0.045	-0.51 ± 0.065	-0.59 ± 0.20	II

Note. — Only No. 2 is detected in GLIMPSE catalog/archive at 8 μm. Others use *MSX* A magnitudes.

Table 4. Comparison of Classified Sources in IRDC G53.2 and Control Fields

Class	Number in Control Fields	Number Scaled to Area of IRDC G53.2	Number Identified in IRDC G53.2	Contamination Fraction
I	2	0.9	76(2)	1.2%
Flat-spectrum	6	2.8	66	4.2%
II	13	6.1	133(2)	4.6%
III	61	28.5	62	45.9%
Photospheric	136	63.5	26	∼100%

Note. — The sources of IRDC G53.2 (column 4) only account for the sources in Table 2, and the numbers of the MIPS-saturated sources (Table 3) are presented in parentheses for reference. Note that including the MIPS-saturated sources does not affect the fraction of field star contamination (column 5).

Table 5. Comparison of Number Ratio of Class II to Class I Objects ($N_{\rm ClassII}/N_{\rm ClassI}$) between IRDC G53.2 and Other Star-forming Regions

Region	Distance (kpc)	Without Correction	$\alpha_{2-24\mu{\rm m}}$-based Class	At 1.7 kpc[a]
IRDC G53.2[b]	1.7	0.9	0.9	0.9
Gutermuth et al. (2009)	<1	3.7	2.0	0.8
c2d clouds[c]	<0.3	2.1	2.1	1.1
Vul OB1[d]	2.3	1.9	1.2	∼1.2[e]

[a]Classification is based on $\alpha_{2-24\mu{\rm m}}$.

[b]The numbers are after removing field star contamination.

[c]Evans et al. (2009)

[d]Billot et al. (2010)

[e]Since Vul OB1 is at the similar distance to IRDC G53.2, we use $N_{\rm ClassII}/N_{\rm ClassI}$ without correction.

Table 6. Numbers of Young Stellar Object Candidates in IRDC G53.2 in the *Herschel* 500 μm Contours

Class	8 Jy beam^{-1}	5 Jy beam^{-1}	3 Jy beam^{-1}	2 Jy beam^{-1}	all IRDC[a]
I	15 (19%)	33(42%)	56(72%)	74(95%)	78(100%)
Flat-spectrum	4 (6%)	18 (27%)	36 (55%)	53 (80%)	66 (100%)
II	11 (8%)	30 (22%)	54 (40%)	84 (62%)	135 (100%)
III	0 (0%)	0 (0%)	2 (3%)	15 (24%)	62 (100%)
$N_{\rm ClassII}/N_{\rm ClassI}$[b]	0.6	0.6	0.6	0.7	0.9

[a]The numbers without removing field star contamination.

[b]Flat-spectrum is included in Class I.

Table 7. NN2 Distances of YSO Candidates in IRDC G53.2

Class	I+Flat	II	III
Median NN2 distance (pc)	0.24	0.38	0.68
70% of cumulative dist. (pc)[a]	0.33	0.54	0.73
80% of cumulative dist. (pc)[a]	0.46	0.68	0.98

[a]NN2 distance where 70% or 80% of the sources are included in normalized cumulative distribution.

Table 8. Kolmogorov−Smirnov Probabilities of the Normalized Cumulative Distributions of the NN2 Distances between Each YSO Class

Class	I+Flat	II	III
I+flat	···	9×10^{-3}	8×10^{-12}
II	9×10^{-3}	···	1.7×10^{-4}
III	8×10^{-12}	1.7×10^{-4}	···